Remote Sensing of Environment 305 (2024) 114096

Contents lists available at ScienceDirect

Remote Sensing of Environment

journal homepage: www.elsevier.com/locate/rse

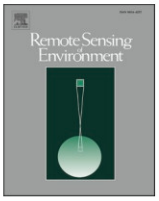

Detecting early winter open-water zones on Alaska rivers using dual-polarized C-band Sentinel-1 synthetic aperture radar (SAR)

Melanie Engram [a,*], Franz J. Meyer [b], Dana R.N. Brown [c], Sarah Clement [c], Allen C. Bondurant [a], Katie V. Spellman [c], Laura E. Oxtoby [a], Christopher D. Arp [a]

[a] Water and Environmental Research Center, Institute of Northern Engineering, University of Alaska Fairbanks, USA
[b] Geophysical Institute, University of Alaska Fairbanks, USA
[c] International Arctic Research Center, University of Alaska Fairbanks, USA

ARTICLE INFO

Edited by Menghua Wang

Keywords:
River ice
Synthetic aperture radar (SAR)
Sentinel 1
Northern rivers
Citizen science
Climate change

ABSTRACT

Northern high-latitude river ice provides critical natural infrastructure for winter travel, commerce, hunting, fishing, and recreation in rural areas with little or no road access. Open water zones (OWZs) in river ice are dangerous for such travel and are most common during early winter. Changes in the occurrence and duration of OWZs may also indicate more widespread shifts in ice regimes across Alaska and other northern regions. To aid in detecting open water hazards and broader changes in winter conditions, we developed a supervised classification with a principal component analysis (PCA) using both polarizations of Sentinel-1 C-band synthetic aperture radar (SAR) dual-polarized data for rivers in early winter to discriminate between ice cover and open water. Previous SAR river ice classifications have focused on one or two river reaches often with an emphasis on moving ice during spring break-up, hampering generalization of these results to other rivers and seasons. To address this limitation, we used 12 reaches from eight rivers for training and validation with the aim to combine data from different river types to create an ice classification that could be applied to northern high-latitude rivers from October through January. The classification was trained using shore-based time-lapse photos, aerial photos, and on-ice observations, and validated with shore-based time-lapse photos and independent citizen scientists' photo observations. Overall accuracy for the classification ranged from 65 to 93% with a corresponding range of 0.31–0.84 Cohen's Kappa statistic ($\hat{K}$). We report some ambiguity between open water and smooth ice, especially in slower-flowing parts of rivers. We conclude that VV and VH thresholds can therefore be customized to increase accuracy, depending on specific river attributes such as river morphology, silt/sediment load, and channel flow velocity. This classification, which allows for mapping long river reaches in low-light winter conditions, can be performed on historical Sentinel-1 imagery to determine areas that display open water year after year. Once customized to a particular river, it can be automated to provide current open water zone maps to Alaskan and other rural northern communities worldwide to aid safer travel on ice.

1. Introduction

Ice-covered rivers are rural Alaska's winter highways and provide snowmobile and dog mushing access to the off-road-system villages and towns which comprise the majority of communities in the state and are typical of high-latitude regions across the pan-Arctic. Ice-covered rivers also serve as foundations for ice bridges, ice roads for vehicles, and as runways for ski-planes in northern high-latitude rural communities. Arctic warming has changed the ways rivers freeze and has impacted rural winter river travel due to later freeze-ups, mid-winter open water zones (OWZs), and earlier break-ups (Brown et al., 2023; Brown et al., 2018; Knoll et al., 2019; Prowse et al., 2011; Yang and Zhang, 2022; Yang et al., 2020). Travel safety is compromised as OWZs become more common and appear in new locations due to intensified warming in the Arctic (Cold et al., 2022; Herman-Mercer et al., 2011; Schneider et al., 2013; Wilson et al., 2015). Permafrost thaw in Alaska (Hinzman et al., 2005; Romanovsky et al., 2010) has increased winter ground water contributions to major Alaska rivers (Brabets and Walvoord, 2009; Ge et al., 2013; Walvoord and Striegl, 2007) and may also create persistent OWZs in northern river ice.

* Corresponding author.
E-mail address: melanie.engram@alaska.edu (M. Engram).

https://doi.org/10.1016/j.rse.2024.114096
Received 8 November 2023; Received in revised form 5 February 2024; Accepted 1 March 2024
Available online 13 March 2024

Monitoring the progression of river freeze-up and detecting persistent OWZs has been approached from multiple perspectives (Lindenschmidt, 2020). Our research is focused on rural northern communities' need for information on river OWZs, and, to that end, we engaged community members in deploying and maintaining shore-based cameras and sharing photographic observations. This has shown to be advantageous on many levels (Eicken et al., 2021; Goldstream Group, 2022): 1) local community members identify areas that are perhaps most important to them, 2) wide spatial distribution of rural Alaska communities is advantageous for comprehensive spatial coverage of observations, and 3) citizen science is a cost-effective method for data collection in remote northern high-latitude regions where logistics are complicated. Fixed shore-based cameras operating alone have been used to gather river-ice information (Ansari et al., 2017), and are useful in providing regular, autonomous repeat photos. Photo observations collected by community members have the advantage of focusing in on river ice open water occurrences that are important to the community beyond the frame of the fixed camera. Satellite imagery can cover entire river reaches with a broader footprint than fixed cameras, record changes in regular time increments, and provide information from remote river locations that are difficult or dangerous to access. However, remote sensing imagery requires validation to ensure proper interpretation of river ice conditions. We used synthetic aperture radar (SAR) remote sensing coupled with shore-based cameras and photo observations from community members to train and validate a SAR remote sensing classification of early winter rivers' surface (ice vs. water).

SAR is an active microwave sensor and can image at night and through clouds, making it a valuable tool for river ice imaging at northern high-latitudes during winter when optical imagery is scarce. The reflected signal (backscatter) that constitutes a SAR image generally depends on the roughness and/or wetness of the target (Meyer, 2019), although imaging parameters such as SAR polarization and incidence angle also affect backscatter. C-band SAR (~5.5 cm wavelength) can penetrate dry snow and ice to interact with the ice-water interface of rivers as long as the surface is dry, although some signal may be reflected from within the ice cover (Fig. 1). Low backscatter occurs with specular reflection, where the signal bounces off a smooth target and travels away from the reception antenna, while high backscatter occurs when it bounces off a rough or wet surface back toward the reception antenna. Early SAR river ice classifications posited that backscatter from river ice was caused by the rough ice-air surface as well as volumetric scattering from gas bubbles, cracks, and impurities in the ice (Unterschultz et al., 2009) or small air bubbles in the ice (Mermoz et al., 2009). However, a backscatter model for river ice, based on wave propagation through media with contrasting dielectric properties, predicted that scattering from the ice-water interface would be the dominant scattering mechanism for VV and VH polarizations over all incidence angles (Gherboudj et al., 2010). The high dielectric constant of liquid water ($\varepsilon' \approx 80$, Skolunov, 1997) creates a high contrast with ice ($\varepsilon' \approx 3.2$, Mätzler and Wegmüller, 1987), causing the ice-water interface to be the most reflective horizon in a river ice profile for SAR (Gherboudj et al., 2010).

Incidence angle (Fig. 1) will affect SAR backscatter (σ^0) from ice and open water in different ways for different polarizations. Measured backscatter from pure ice shows that C-band VV polarized σ^0 is relatively unaffected by incidence angle as opposed to HH σ^0 which decreases sharply as the incidence angle increases, even when imaging the same freshwater ice target (Leconte et al., 2009). This makes VV polarization useful for classifying river ice that can stretch over a single Sentinel-1 scene where incidence angles range from 29°-46°. However, C-band VV σ^0 over open water is more sensitive to wind- and current-caused small waves that roughen river water surfaces than is HH polarization (Long et al., 1996). This results in higher VV σ^0 from rough open water (Long et al., 1996), which can confound the detection of ice vs. open water. VH σ^0 is not as sensitive to small waves on the surface of open water. By using VH in conjunction with VV polarized σ^0 intensity, we aimed to avoid false ice detections due to rough open water that can occur when using only VV polarized σ^0.

While previous empirical studies can apply their results to their specific river reaches, there is currently no SAR river ice classification

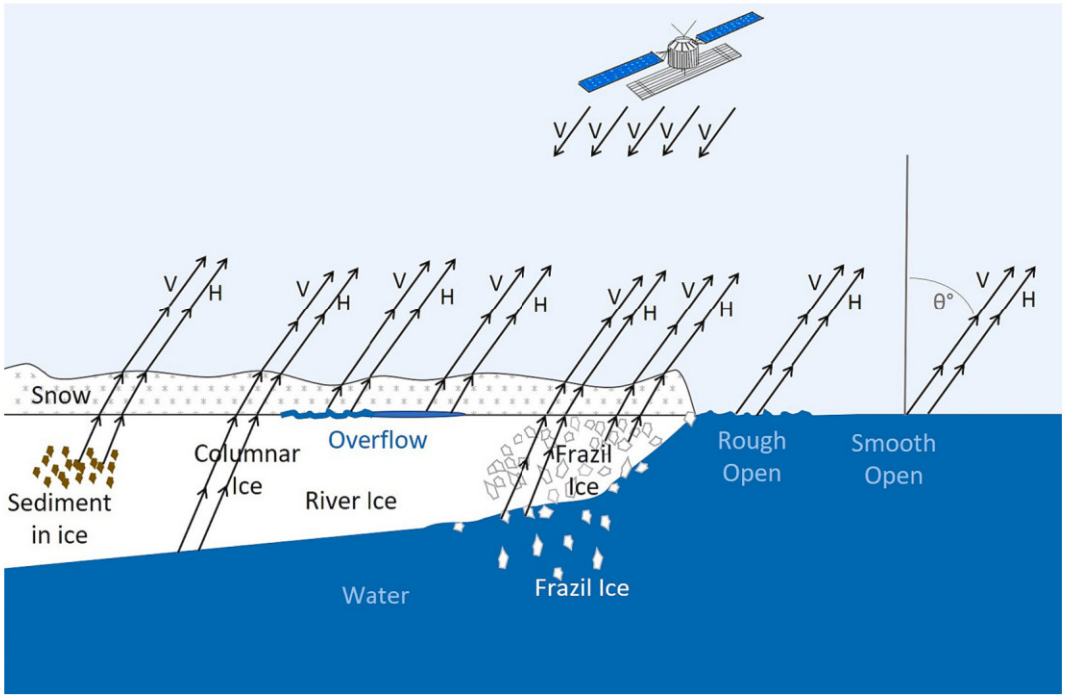

Fig. 1. Some possible scattering features in a northern river ice system. Schematic represents a SAR instrument transmitting in vertical orientation (V) and the target reflecting the wave in the same vertical orientation (V) or depolarizes it to horizontal polarization (H). Incidence angle, represented by theta (θ), considers the curvature of the earth as well as satellite look angle. The origin of the returning arrows illustrates the probable depth of penetration based on dielectric constants of the targets but does not indicate backscatter magnitude nor direction. Bent arrows indicate direction of refracted wave through the media of snow and ice.

that can be generalized and expanded to use the freely available Sentinel-1 VV/VH polarized data across the northern landscape, especially in early winter. In previous imaging efforts of Canadian rivers, HH-polarized SAR data was used to monitor ice jams and flooding risk (Gauthier et al., 2006; Łoś et al., 2016; Łoś et al., 2019; Mermoz et al., 2009; Unterschultz et al., 2009; Van der Sanden and Drouin, 2011; Van der Sanden et al., 2021; Weber et al., 2003) as well as travel hazards (Gauthier et al., 2010). Quadrature-polarized (quad-pol) Freedman-Durden decomposition has been used for the Slave River, with an emphasis on determining structural strength for river ice travel (Lindenschmidt and Li, 2018). Previous SAR-river-ice classification work using VV/VH C-band SAR (Sentinel-1) focused on one or two rivers in temperate climates with little or no underlying permafrost or glacial silt load: Stonevicius et al. (2022) trained a VV and a VH classification threshold for river ice on the Nemunas and Neris Rivers in Lithuania (54–55°N latitude), and de Roda Husman et al. (2021) used Sentinel-1 for the Athabasca River in Canada (56.6° N latitude), examining breaking ice later in the winter.

Results from these studies cannot be applied with confidence to northern high latitude rivers in early winter since they were empirically developed based on only one or two river reaches, sometimes at temperate latitudes, and often focused on late winter/spring breaking ice. Further, the use of HH- or quad-polarized data limits transference to VV/VH polarized SAR that Seninel-1 uses. To address this shortcoming, we present a classification using the first principal component of VV and VH polarizations from Sentinel-1 C-band SAR using data from 12 river reaches representing a variety of northern river types.

This method assesses VV and VH values for each pixel, considering the intensity of each polarization returned from open water and from ice, to create a bi-conditional SAR river ice classification. Our emphasis is on open water as a travel hazard during river freeze-up from October through January, a timeframe when OWZs are likely to hinder safe travel, though this technique could be applied to other timeframes. Our main objective was to create a generalized C-band SAR river ice classification that could be applied operationally to Alaskan and other northern rivers >60° latitude coursing through differing extents of permafrost, by using sites and data from rural community members. This classification should be straightforward enough to be used by operational users and scientists, and should be easy to customize to individual rivers. Our second objective was to assess the accuracy of this classification, especially to detect OWZs in river ice, looking for relationships between classification accuracy and river attributes to examine where these data show the distinction between river ice and open water the best and where it can separate classes better than others. Our third objective was to assess the effect of incidence angle on a SAR river ice classification using VV and VH polarizations, in order to ascertain classification integrity across the broad range of incidence angles used by Sentinel-1 to image long river reaches.

2. Methods

2.1. Study sites and design

Of the four Alaska river reaches used to train our classification, three were large multi-channel rivers (the Yukon, Kuskokwim, and Tanana Rivers) and one was a smaller, single-channel, deeper river (the Innoko River) (Fig. 2, Table 1). We compared shore-based camera images in early 2019–2020 winter to both channels (VV and VH) of Sentinel-1 dual-polarized SAR data. The solar-powered shore-based cameras (Nupoint remote viewer Lite Sight Rapid Pack) took an oblique photo once daily at near noon local time to capture river surface conditions at the brightest time of the winter day. In addition to shore-based cameras, in situ observations on the Tanana River between Fairbanks and Nenana from late January 2021 were used to train the SAR classification. We used a principal component analysis (PCA) to establish VV and VH intensity thresholds for a SAR classification of open water and river ice

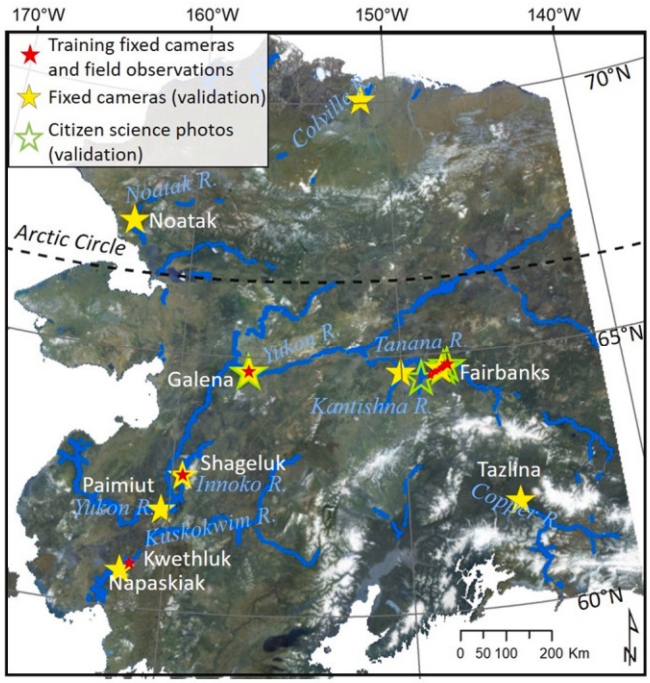

Fig. 2. Red stars mark locations of training camera locations (early winter 2019–2020) and 97 field observations on the Tanana River downstream from Fairbanks (January 2021). Yellow stars show validation camera locations (early winter 2020–2021). Green star outlines show locations of citizen observations for validation on the Tanana, and Yukon, Rivers (early winter 2020–2021). Background image: Alaska High Resolution Imagery RGB 2020 (Maxar Technologies Inc., Alaska Geospatial Office, USGS). (For interpretation of the references to colour in this figure legend, the reader is referred to the web version of this article.)

cover and then validated this supervised classification with early winter 2020–2021 shore-based photos from remote cameras on eight Alaska rivers (Fig. 2, Table 1, Bondurant et al., 2022). We also used citizen science observations taken by community-based monitoring teams or individuals and uploaded to the Fresh Eyes on Ice Observer portal (https://obs.feoi.axds.co/observations/) for the Tanana and Yukon Rivers to validate our classification and assess its accuracy.

2.2. River characterization

The locations of training and validation shore-based cameras were chosen to capture a variety of river types with different characteristics, including: large and small rivers; different river bed morphologies (multi- or single-channel: braided, anastomosing, straight, meandering); glacial-fed, non-glacial and mixed tributaries; wide and narrow; north-south and east-west orientation; tundra and boreal biomes; and residing in a variety of permafrost conditions. Ice begins forming in these rivers in October or November and remains until May to June, depending on latitude. River morphology was determined manually by viewing the channel form in optical imagery (Table 1). We differentiated between single and multi-channel rivers, and characterized reaches as either meandering, anastomosing, or braided, which vary in their formation processes, channel stability, and sedimentary properties (Makaske, 2001). Meandering reaches are single-chandelled and the most stable, braided reaches are the most dynamic of the multi-channel morphologies and exhibit humped-up bar-like forms between channels, while anastomosing reaches encloses parts of the floodplain between multiple channels. The width of the river at the location of the shore-based camera was measured in ArcMap. Glacial silt contribution was manually determined from optical imagery of each river's headwaters and tributaries and represents a first-order assessment of glacial silt load

Table 1
Characteristics of rivers used for training and validation of SAR ice/open-water classification. Channel form indicates river reach at the location of shore-based camera or citizen observation. Permafrost extent from Jorgenson et al. (2008). Rivers are listed in order of descending latitude.

River	Nearby Community/ Place Name	Role (Training vs. Validation)	Channel (multi/single) Form[a]	Glacial contribution	River width (m)	Latitude (°N)	Permafrost[b]
Colville	Ocean Point	Valid.	multi A	none	263	70.07	C
Noatak	Noatak	Valid.	multi B	none	204	67.52	C
Tanana	Fairbanks	Train.	multi A	high	268	64.79	I
Yukon	Galena	Train. & valid.	multi A	high	774	64.73	S/I
Tanana	Sam Charley Is.	Valid.	multi A	high	282	64.72	I
Kantishna	Tolovana Roadhouse	Valid.	multi A	medium	181	64.70	I
Innoko	Shageluk	Train. & valid.	single M	low	146/186	62.65	S
Copper	Tazlina	Valid.	multi B	high	260	62.02	I
Yukon	Paimiut	Valid.	multi A	high	974	61.96	D/I
Kuskokwim	Kwethluk	Train.	multi A	medium	341	60.86	I
Kuskokwim	Napaskiak	Valid.	multi A	medium	683	60.72	I

[a] A = anastomosing, B = braided, M = meandering.
[b] C = continuous, D = discontinuous, S = sporadic, I = isolated.

from glacial melt. We also aimed to represent a variety of regions and permafrost conditions, and installed shore-based cameras in Alaska's north slope, interior, southwest, and south-central regions in continuous, discontinuous, sporadic, and isolated permafrost (Jorgenson et al., 2008) with the goal that our results could be applied to a variety of northern rivers worldwide. We compared all quantitative river characteristics to our SAR classification accuracy, checking latitude, river width, and number of observations for correlations with classification accuracy.

2.3. SAR dataset

Sentinel-1 carries a C-band SAR instrument with a ~ 5.4 cm wavelength, which is a useful SAR frequency for freshwater ice classification as demonstrated by earlier missions such as ERS-1/2, RADARSAT-1/2, and ENVISAT (Bartsch et al., 2017; Engram et al., 2018; White et al., 2008). Frequent dual-polarization (dual-pol) Sentinel-1 SAR scenes acquired with vertical transmit and receive (VV) coupled with vertical transmit and horizontal receive (VH) polarizations are readily available worldwide in Interferometric Wide (IW) swath mode, due to open access policy of the European Space Agency (Torres et al., 2012). Each Sentinel-1 IW mode pass covers a 250 km wide area with a pixel spacing of ten meters (Torres et al., 2012). The exact-path repeat time is 12 days, but overlapping orbits at high-latitudes and the combined orbits for Sentinel 1 A and 1B allow for more frequent images albeit with differing incidence angles and flight directions (ascending and descending passes). To develop and validate a river ice classification for Alaska, we used all Sentinel 1 IW Level 1 ground range detected (GRD) data from Sentinel 1 A and Sentinel 1B in early winter (from Oct. 1 to Jan. 31) over training sites for 2019–2020 with one January 2021 scene (Supplemental Table 1) and over validation sites for 2020–2021 (Supplemental Table 2).

2.4. SAR image processing

Data were downloaded from the Alaska Satellite Facility's Vertex interface and processed using the Sentinel-1 toolbox in the Sentinel Applications Platform (SNAP) toolset (v7 and v8) freely provided by the European Space Agency. Precise orbits were applied, thermal noise reduction performed, the Lee Sigma speckle filter was applied (Lee et al., 2009) and data were calibrated to sigma-naught backscatter (σ^0). Terrain-correction was implemented using the Global Earth Topography and Sea Surface Elevation at 30 arc-second resolution (GETASSE30) elevation model available in SNAP for all rivers except the Innoko and Copper rivers where steep terrain required the more precise correction provided by the IfSAR digital terrain model (DGGS, 2013). The Copernicus GLO-30 DEM was not available in SNAP when these data were processed. Data were then projected to the Alaska Albers map projection with ten-meter pixel spacing in a geo-tiff file format for GIS analysis in ArcMap (v10.7). Incidence angles at the locations of shore-based cameras and in situ sample locations were determined from each scene in SNAP.

2.5. Supervised classification training sampling

To compare SAR σ^0 values from river ice/open conditions at the locations of shore-based cameras' field of view (FOV) on the four Alaska training rivers (Table 1), we first digitized river shorelines using very high-resolution optical imagery from Planet (Planet, 2017), using the last image before freeze-up to omit highly reflective sandbars exposed in late fall when river water level drops. We created shore-based cameras' FOV polygons in ArcMap (v. 10.7) using landmarks along the shores, then used the FOV polygons to select SAR pixels from both VV and VH polarizations in SAR (Fig. 3). For photos where there were both water and ice in the camera's FOV (ex. Innoko R. at Shageluk late 2019), two separate polygons were digitized, again using shore-based landmarks, and the open water polygons were only used on imagery acquired when open water or steam was clearly visible in the shore-based camera image.

State of the river as "open", "skim ice", "pan ice", "rough ice", "smooth ice", "wet rough/smooth ice" were manually determined from shore-based camera images closest to SAR acquisition times, although we later simplified this fairly complex ice-type delineation. We constructed a time series for our four training river reaches by calculating the mean and standard deviation of each VV and VH σ^0 for the shore-based camera's FOV for each SAR scene (Fig. 3). Skim ice was defined as a thin film (~ < 1 cm) of ice moving down the river on the water, not necessarily completely covered but was later combined with open water since σ^0 intensities from skim ice and open water were indistinguishable. Pan (frazil pan) ice could be considered open water with moving ice. The number, size, and texture of the pans can change from minute to minute, thus invalidating any comparison with SAR imagery acquired hours later: pan ice was therefore omitted from the classification. Smooth and rough ice categories described the top surface of the ice, sometimes covered with snow, once a static ice cover was established. We explored distinguishing wet from dry ice to see if there was a difference in σ^0 but later aggregated these groups when no notable difference was found. We used a combination of "rough ice" and "smooth ice" as well as "open water" to train our four-state classification scheme of "ice", "open water", "less certain ice" and "less certain open water".

We expanded training samples to include one area of smooth ice and two OWZs on the Kuskokwim River that were near our shore-based camera but were outside the FOV, using aerial photos taken by the Bethel Search & Rescue (Guest, 2019) on Nov. 18 and Dec. 3, 2019 and comparing them with SAR imagery acquired between the two flight dates on Nov. 24 and 25, 2019 (Fig. 4). Additionally, we used 97 in situ

Fig. 3. Shore-based camera installation (a) and ice type examples from shore-based photos: pan ice (b) and rough ice cover (c) on the Tanana R.; skim ice (d) and smooth ice (e) on the Innoko R.; and wet, rough ice on the Kuskokwim River (f). Panel g shows training camera location on the Kuskokwim River (white camera icon) with approximate range of view in white and SAR pixel sampling area outlined in black. Green stars in panels f and g show the same location. Photo credit (a) C. Arp. Background image (g): Alaska High Resolution Imagery RGB 2020 (Maxar Technologies Inc., Alaska Geospatial Office, USGS). (For interpretation of the references to colour in this figure legend, the reader is referred to the web version of this article.)

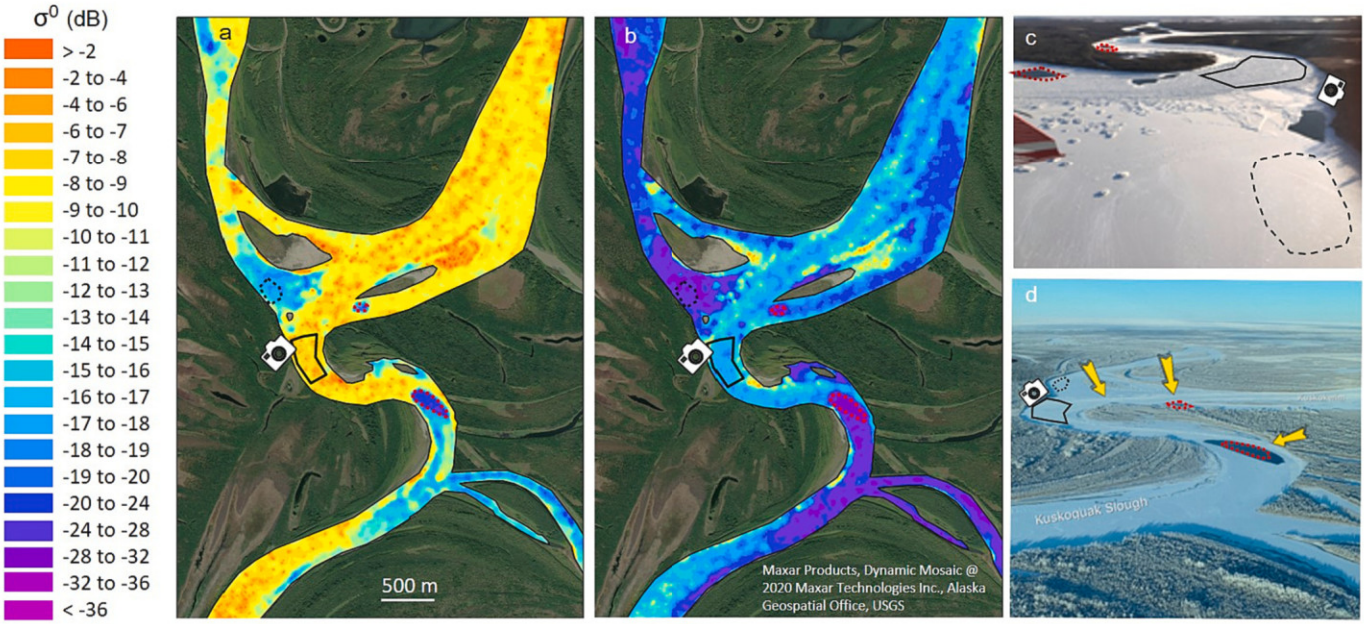

Fig. 4. Kuskokwim R. above Kwethluk. Panel (a) and (b) show VV and VH Sentinel-1 intensity, respectively, for Nov. 24, 2019 (Copernicus Sentinel data 2019, processed by ESA). Panel (c) and (d) show aerial photos from Bethel Search and Rescue from Nov. 18 and Dec. 3, 2019, respectively. Each panel shows the location of shore-based camera (camera icon), the pixel sampling area which was classified as "rough ice" (black solid line), smooth ice (black dashed line), open water (white dashed lines). Photo credit C. Guest.

observations from a section of the anastomosing Tanana River from Jan. 26–29, 2021 between Fairbanks and Nenana, AK, recording the location of smooth ice, rough ice, and open water conditions with Garmin hand-held GPS units. During field work, cold air temperatures of −32 °C created rising steam from open water areas and facilitated open water detection downstream from Fairbanks along a ~ 35 km section of the river SW of Sam Charley Island. We compared these field observations with σ^0 from the temporally closest SAR scene (Jan. 25, 2021 @ 6:21 pm local time). SAR intensity values were extracted in ArcMap for these locations using the GPS coordinates for points and bilinear interpolation of the four nearest pixels, weighted by distance from the point.

While shore-based cameras on all four rivers provided data from one location at high temporal resolution, the in-situ data provided broader spatial sampling from one river with low temporal resolution (only one image). Altogether 140 examples of ice and 26 observations of open water were used to train the SAR VV and VH ice classification.

2.5.1. *Determining SAR threshold dividing ice and open water using PCA*

Our sample sizes were not equivalent: we had more pixels from rough ice than from open water or smooth ice. We used all ~1250 pixels from smooth ice and randomly selected an equivalent number of pixels for rough ice (1262) from our larger rough ice pixel pool, using the random number generator in Excel software (v. pro-2019) resulting in a ~ 2500-pixel dataset of "ice" (Table 2). Using the same random selection method, we chose an equivalent number of open water pixels (2596) in preparation for a statistical analysis of SAR σ^0 from ice (50% rough and

Table 2
Mean backscatter from all training pixels from four rivers randomly sub-sampled to create equivalent sample sizes.

Class	n pixels	Mean VH (dB)	Stdev VH (dB)	Mean VV (dB)	Stdev VV (dB)
Open water	2596	−27.3	1.5	−19.6	2.7
All Ice	2515	−21.5	5.3	−11.9	4.5
Smooth Ice	1253	−26.1	2.3	−16.1	1.6
Rough Ice	1262	−16.9	3.0	−7.8	2.1

smooth) vs. open water (Table 2).

Since VV and VH were highly correlated, we performed a PCA using VV and VH intensity values from river ice and open water using NumXL software (v. 1.68.544979), effectively rotating the dataset along the least-squares regression line prior to determining a threshold between these overlapping classes. We tested the first principal component, PC1, frequency distributions of all classes (all ice, smooth ice, rough ice, open water) for normality (NumXL v. 1.68.544979). We then used the PC1 values with Eq. 1 to determine the threshold to divide all ice from open water, resulting in equal classification error from two normal distributions (Engram et al., 2018),

$$Threshold = \mu_1 + \lfloor \frac{\mu_2 - \mu_1}{std_1 + std_2} * std_1 \rfloor \quad (1)$$

where μ_1, std_1 and μ_2, std_2 are the mean and standard deviation of open water-PC1 and ice-PC1, respectively. We converted the PC1 threshold back to VV and VH components, creating a line through this threshold with a slope orthogonal to the original regression equation to divide pixels into ice and open water. Using the x- and y- intercepts to draw an orthogonal line ($VV_{dB} = -1.0552 * VH_{dB}$ -yint), we determined that a pixel (VH_i, VV_i) was on the right side of the line and classified as ice, if Eq. 2 were true:

$$[xint*(VV_i - yint)] \leq (-yint*VH_i) \quad (2)$$

where *xint* and *yint* are the x- and y-intercepts for the threshold orthogonal line. The pixel (VH_i, VV_i) would be on the left (lower) side of the line and classified as open water if Eq. 2 were false. Kernel density plots were created in Origin software 2023b (v. 10.0.5.157). To account for the considerable overlap between some smooth ice and open water, we also outlined a "less certain" category where the following two conditions both existed: 1) VV was higher than 95% of all ice pixels, and 2) VH was lower than 95% of all open water pixels that satisfied the first condition.

2.5.2. Validation and accuracy assessment

We validated the resulting river ice classification using 160 images from shore-based cameras along eight Alaska rivers from Oct. 1, 2020 to Jan. 31, 2021, and with community observations from submitted photos to the Fresh Eyes on Ice Observer portal (https://obs.feoi.axds.co/) during that time frame. Validation shore-based cameras acquired daily near noon local time photos for the Colville, Noatak, Tanana, Kantishna, Innoko, Kuskokwim, Yukon (at Galena and at Paimiut), and Copper rivers (Table 1). One camera stayed in the same location as the previous year (Galena) and the other eight cameras were mounted in new locations to capture the 2020–21 freeze-up (Fig. 2). Citizen science observations consisted of oblique shore-based photos, the time/date taken, and map location where they were observed. We used all citizen science observations that were made on the same day as a SAR acquisition, omitting two observations showing OWZs smaller than one SAR pixel. We also included two citizen's observations that were noted to be persistent OWZs, using the SAR scenes that had been acquired closest in time for validation. Altogether five citizen science observations were used.

We compared these observations with all SAR data from both ascending and descending passes from Oct. 1, 2020 – Jan 31, 2021 (Supplemental Table 2), processed to σ^0 intensity images in SNAP (as described in Section 2.2) and classified to show four classes: ice, open water, less-certain ice, and less-certain open water. Classification was performed with a Python script (available in GitHUB) in ArcMap (v10.7). Autumn river perimeters and camera FOV polygons for validation were established using the same methods as for training data.

Photos from shore-based cameras and from citizen science observations were too oblique to be rectified in ArcMap and we therefore could not perform a pixel-by-pixel classification accuracy assessment. Instead, we performed a case-by-case accuracy assessment, matching ice conditions in the photos with SAR classification results in the shore-based camera's field of view (FOV), where a "case" is an instance of either ice or of open water: when the river shows all ice or all open water, one case exists but where there is both ice and open water in the shore-based camera photo, two cases exist. We validated SAR classification results using cases of water and ice according to the rubric outlined in Fig. 5.

Instances when the shore-based camera lens was obscured by snow or ice, as well as areas of ambiguity within a shore-based camera image (dark areas could be either wind-blown ice or open water in the far field of view), were classified as "no data" and omitted from validation. Additionally, since pan ice is a very dynamic state and SAR scenes were not acquired at the same moment as the shore-based camera scene, pan ice was therefore omitted when validating this SAR classification.

2.6. Incidence angle as a factor

We investigated incidence angle as a factor in σ^0 because we saw a ~ 1–4 dB difference in VV σ^0 from ice with incidence angles ranging from 33 to 44° although data were acquired from one to three days apart on the Tanana River at Fairbanks (Fig. 6). Additionally, Łoś et al. (2016) called for further investigation on the influence of incidence angle for different river ice types. We used σ^0 because it has been the ground-range convention in SAR since it is ellipsoid-based (Small, 2011). However, gamma-naught (γ^0) will produce a radiometric flatter scene across varying incidence angles when corrected with an accurate digital elevation model: the two ground-range calibrations are related with $\sigma^0 = \gamma^0 * \cos\theta$ (Small, 2011). The incidence angle at each of our training locations were recorded from SNAP software at the latitude and longitude of the shore-based camera FOV in each scene, then mean σ^0 and standard deviation of pixels sampled from the FOV in each scene were calculated and plotted against SAR incidence angle. Data were checked for statistical correlation (SPSS v.25) between incidence angle and σ^0 for rough ice, smooth ice, and open water.

3. Results

3.1. Backscatter intensities from ice and open water

The time series for training data using shore-based cameras show low σ^0 in both VV and VH from open water in October prior to freeze-up, then higher σ^0 for VV and VH from ice after freeze-up, especially from rough ice (Fig. 6). As the rivers start to freeze, floating pans of frazil ice on open water (pan ice) are observed in shore-based photos on the Yukon, Tanana, and Kuskokwim Rivers, resulting in rough ice with frazil ice inclusion once the river freezes to a static ice cover. Smooth ice in the slower flowing Innoko River is probably columnar ice (inferred from the lack of pan ice) and shows less of a σ^0 contrast from open water than does rough ice on the other three rivers. The two smooth ice points on the Kuskokwim River are lower in both VV and VH than the smooth ice on the Innoko River (red symbols, Fig. 6).

Note that σ^0 from pan ice is highly variable, overlapping the range of σ^0 from open water as well as ice. This large variability in σ^0 from pan ice is most likely due to differences in pan density, a dynamic condition that could not be compared to SAR backscatter when captured by shore-

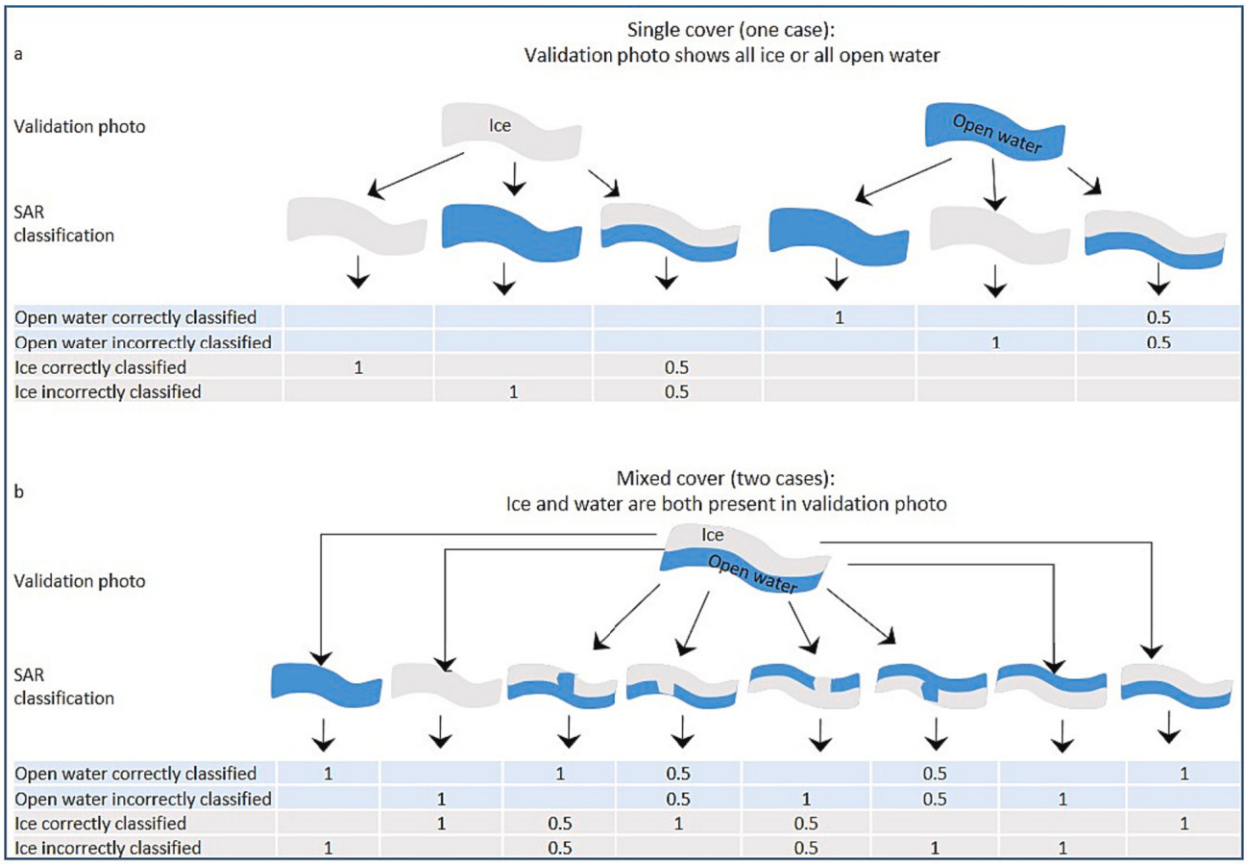

Fig. 5. Schematic shows accuracy scoring rubric for SAR classification using validation photos. Curved shapes represent river surfaces with ice (grey) and open water (blue). If the validation photo of river surface shows either all ice or all open water (a), this is considered as one case (only one type of surface on the river): the SAR classification either agrees /disagrees completely, or is partially correct. When there is both ice and water in the validation photo, there are two cases (two types of surface on the river) and eight possible outcomes when comparing the photo to the SAR classification (b). We assigned "1" when **all** ice or open water were correctly identified, "0.5" when only **some** ice or open water were correctly identified. (For interpretation of the references to colour in this figure legend, the reader is referred to the web version of this article.)

based camera photos taken hours earlier than SAR acquisition.

Mean σ^0 from open water pixels (combined training data from the four rivers) was low with −20 dB for VV and − 27 dB for VH (Table 2). Mean σ^0 from rough ice in all rivers was high for both VV (−8 dB) and VH (−17 dB) polarizations at the training locations (Table 2). Backscatter from smooth ice for all training data pixels was generally lower than that of rough ice with mean VV (−16 dB) and VH (−26 dB), (Table 2, Fig. 7a, b).

Backscatter in VV and VH polarizations for pixels of rough ice, smooth ice, and open water from the four training rivers are highly correlated: $VV_{dB} = 0.95*VH_{dB} + 7.34$, $r^2 = 0.74$, $p < 0.01$ (Fig. 7a). A kernel density plot of these data reveals a bimodal aspect to both the smooth ice and open water classes, as well as a substantial overlap between smooth ice and open water (Fig. 7b). The density plot of VH vs. VV (Fig. 7b) also shows a horizontal orientation to the smooth ice density contours and a vertical orientation to the open water density contours. Plotting the results of the principle component analysis as PC1 vs. PC2 effectively rotated the data along the axis of greatest variance for the scatterplot (Fig. 7c) and kernel density plot (Fig. 7d).

3.2. SAR backscatter distributions and thresholds

The first principal component (PC1) frequency distributions (Fig. 8) for rough ice, smooth ice, all ice, and open water all demonstrated normality according to the Jarque-Bera test which emphasizes goodness of fit with skew and kurtosis matching a normal distribution (scores: open water = 2.13, all ice = 1.95, smooth ice = 2.81, and rough ice =3.17). Additionally, the PC1 frequency distribution for open water passed the Kolmogorov-Smirnov normality tests (Lilleifors corrected significance value was 0.14, greater than required 0.05). In addition to the Jarque-Bera test, the PC1 frequency distribution for 'all ice' was considered normal with the Shapiro-Wilk test, the Doornik-Hansen Chi-Square test, and barely failed normality with the Kolmogorov-Smirnov test with a Lilleifors corrected significance value of 0.048 (0.05 is needed to pass normality test). We believe these test results indicate that we cannot completely reject normality for all ice or open water, and that a parametric technique to determine the threshold is appropriate. Additionally, the skewness (0.19 for all ice and 0.595 open water) and kurtosis (−0.975 for all ice and − 1.14 for open water) values are quite reasonable compared to a normal distribution. Alpha value was 0.05 for all normality tests. Using the equivalent sized samples of pixels for ice and open water (Table 2), the PC1 threshold to delineate open water from ice using Eq. 1 was determined to be −0.4869 (Fig. 8b). When this PC1 value was converted back to VV and VH intensity values, the result was a dividing threshold line orthogonal to the least square regression line with the equation.

$$VV_{dB} = -1.055^{*}\ VH_{dB} - 45.244 \quad (3)$$

where pixels to right (higher) of this line are classified as ice and to the left (lower) are classified as open water (Fig. 9).

We outlined a less-certain category for the overlap of open water and smooth ice (Fig. 9) where 1) VV was higher than −19.34 dB (95% of all ice pixels), and 2) VH was lower than −25.52 dB (95% of all open water pixels that satisfied the first condition). Our decision to use percentages

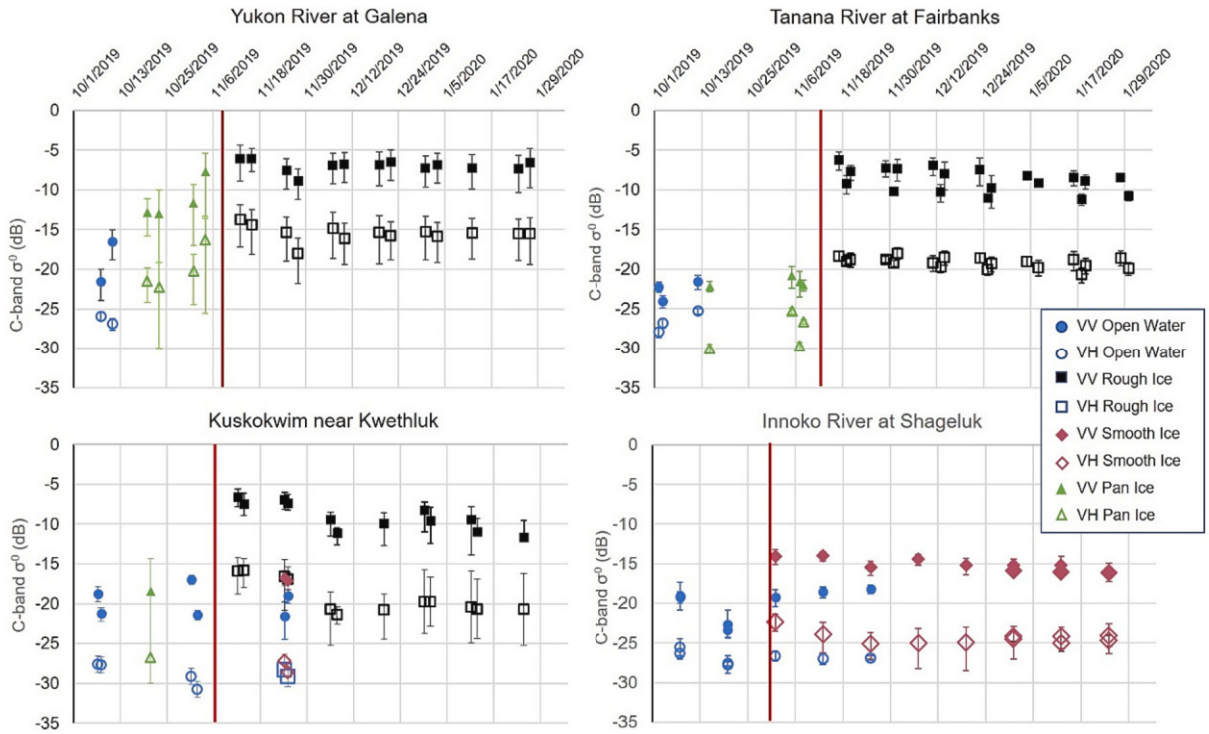

Fig. 6. Time series showing mean σ^0 from FOV of shore-based cameras on the four training river reaches for both the VV (solid symbols) and VH (open symbols) polarizations. Vertical red line indicates freeze-up date when a static ice cover was formed, as determined by ice features in the shore-based cameras appearing in the same location. Error bars are standard deviation. (For interpretation of the references to colour in this figure legend, the reader is referred to the web version of this article.)

of VV and VH as criteria for less-certainty was based on the horizontal (VV) and vertical (VH) orientation of smooth ice and open water data (Fig. 7b).

We therefore finished with the following four classes: ice, less-certain ice, open water, and less-certain open water (Fig. 9) for early winter (Oct.-Jan.) river ice classification. These classes are statistically based on both the VV and VH σ^0 backscatter from 5111 pixels in our training dataset (Table 2), trained with shore-based camera and citizen scientist photos, and in situ observations.

3.3. Classification accuracy for different rivers

Our analysis covered a wide range of river forms and sizes, glacial silt contributions, and latitudinal and permafrost settings (Table 1). The single-channel river width was 186 m while multi-channel river width ranged from 181 to 974 m. The two Arctic river reaches (north of 66.5°N) were on continuous permafrost while the remaining sub-Arctic reaches wire in discontinuous, intermittent, or sporadic permafrost (Jorgenson et al., 2008).

The accuracy of our PC1 threshold classification varied from river to river (Table 3). Overall classification accuracies ranged from 65 to 93% (mean 78%) across nine reaches on eight Alaska rivers. The Kappa statistic ($\widehat{K}$) for our accuracy assessment, a more stringent measure of accuracy that removes random agreement, ranged from 0.31, indicating fair agreement, to 0.84 indicating almost perfect agreement (Table 3). We did not find a statistical correlation between classification accuracy and river width nor with latitude. Rivers that had moderate to almost perfect agreement using the Kappa statistic criteria (Landis and Koch, 1977) had some glacial silt contribution, with the exception of the Noatak River.

3.4. Incidence angle influence on σ^0 from ice and open water

Incidence angles from Sentinel-1 scenes acquired for training sites ranged from 32.5° to 44° and were very similar to those at our validation sites (31°- 45°). Results for our investigation on the effect of incidence angle on our classification showed only weak, slight trends toward lower backscatter with increasing angle. Linear regression slopes of VV and VH backscatter for smooth ice, rough ice, and open water vs. degree (deg) of incidence angle were all negative and relatively flat, ranging from −0.1 to −0.3 dB deg.$^{-1}$ (Fig. 10), indicating a slight decrease in backscatter from the same target with increasing incidence angle. Pearson's r^2 correlation coefficient ranged from 0.0167 to 0.519, indicating weak trends with a high degree of scattering. Correlations had very poor explanatory power, but were statistically significant, in three of the six regressions: VV from rough ice (slope = −0.2 dB deg.$^{-1}$, $r^2 = 0.121$, $p < 0.01$), VH from smooth ice (slope = −0.2 dB deg.$^{-1}$, $r^2 = 0.0464$, $p < 0.05$), and VH from open water (slope = −0.3 dB deg.$^{-1}$, $r^2 = 0.519$, $p < 0.01$).

3.5. Case studies: Yukon and Tanana Rivers

The resulting SAR river ice classification can show ice and open water conditions over long river reaches throughout the winter. Ice formation processes and patterns can be observed using a SAR time series. We present three case studies to compare the SAR classification with the shore camera photos.

Our SAR classification performed moderately well (Table 3) on the Yukon River at Paimuit where the river is relatively straight and wide (974 m, Table 1). The high position of the shore camera at this location provided a steep observation angle, resulting in a more downward-looking oblique photo of the river surface than a lower camera positioned closer to the river's elevation. SAR classification matched the shore camera photo well, showing open water in early October, a fairly well-established ice cover by late October, and an oblong OWZ in early December that was frozen by January (Fig. 11a).

To demonstrate how long reaches of rivers can be classified, we show the Tanana River at Sam Charley Island ~20 river-km SW of Fairbanks.

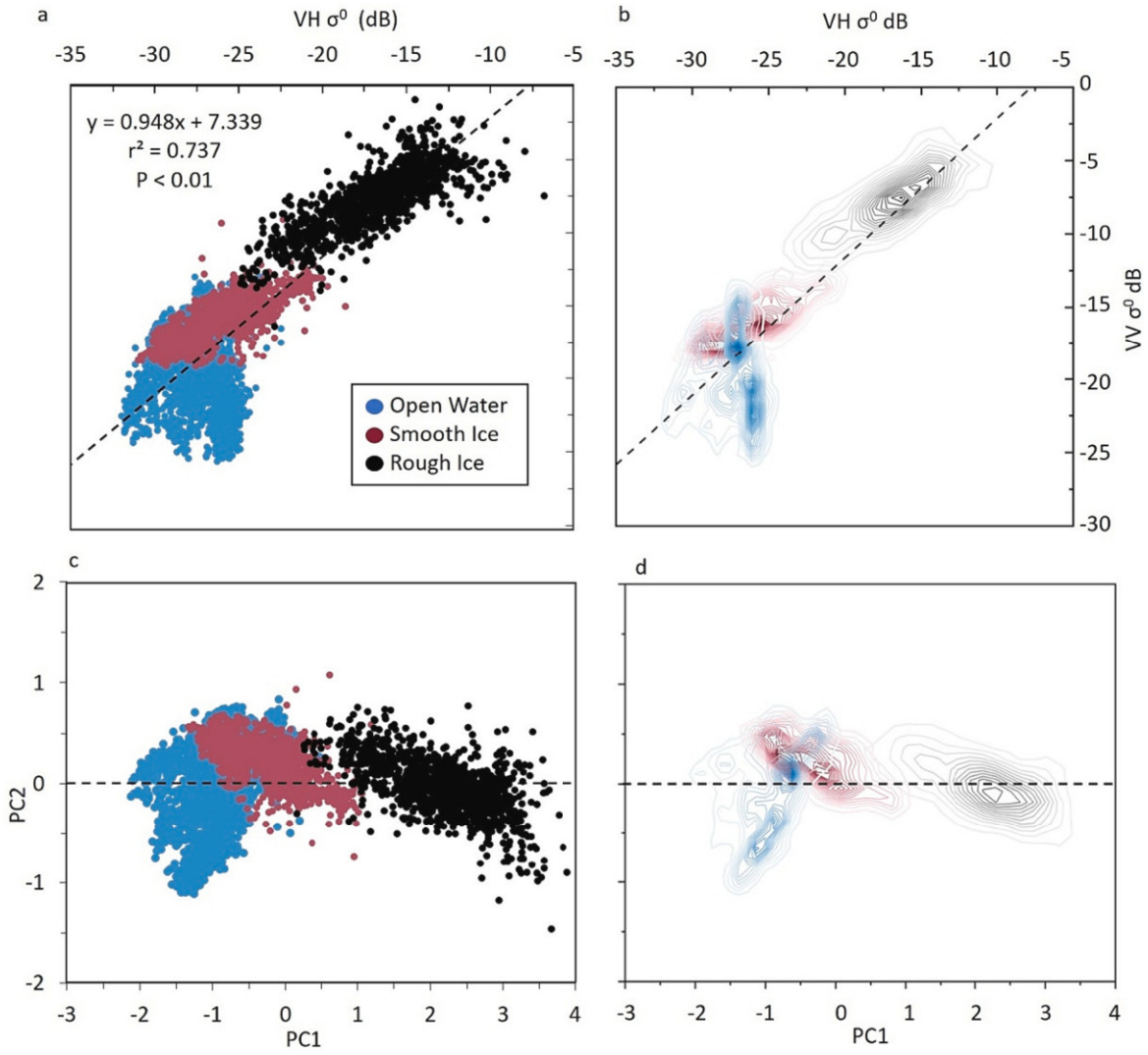

Fig. 7. Scatterplot (a) shows VH and VV from all training data (four river reaches) for open water, smooth, and rough ice are highly correlated, but the extent of overlap and data depth are obscured. Kernel density plot (b) of same data shows density of pixels using contours, revealing the extent of overlap, density of data, and showing a vertical orientation of two lobes of open water and horizontal orientation of two lobes of smooth ice. Principal component analysis effectively rotates the data along the axis of highest variance as seen in the scatterplot (c) and the kernel density plot (d).

Here, the Tanana River is anastomosing, with camera at the junction of a slough and the main river channel. Fig. 11b shows the freeze-up of the Tanana as the SAR classification compares to the shore camera, with completely open water on Oct. 10th, open water in the main channel on Nov. 1, 2020, and an ice cover with no large OWZs in mid-December through late January 2021.

Comparing the freeze-up on these river reaches, the Yukon R. at Paimiut froze earlier than the Tanana R. at Sam Charley Island, despite the Yukon River reach's more southerly location by over two degrees latitude (Table 1). The Yukon River showed more ice in late Oct. 2020 while the Tanana River showed more open water in early Nov. 2020.

An OWZ in the main channel of the Tanana River near the Rosie Creek trail ~12 river-km SW of Fairbanks persisted until late December 2020. On-ice photos taken the same date as the SAR acquisition show the SAR classification performed very well (Fig. 12). Using high bluffs along the Tanana River as landmarks, the SAR classification shows the large OWZ in the same location as the photos (Fig. 12).

4. Discussion

4.1. Toward creating a classification that can be used operationally

We gathered a large pool of data from different types of rivers across a large geographic area north of 60° in Alaska which included a variety of river morphology, river flow velocity, permafrost extent, and glacial/sediment load with the aim to create a generalized ice vs. open water classification that demonstrated fairly good accuracy when tested on nine northern river reaches. By determining thresholding intensity with PCA, then converting PC1 to VV and VH σ^0 values, we created a bi-conditional classification that is statistically-based, yet straightforward for environmental scientists and ice-predicting government agencies to implement with our published Python code. The relatively large number and different types of northern rivers used for training and validation contributed to a general classification that can be applied to other northern rivers with moderate confidence, and possibly fine-tuned for individual rivers.

4.2. Classification accuracy

We looked for trends in classification accuracy relating to river

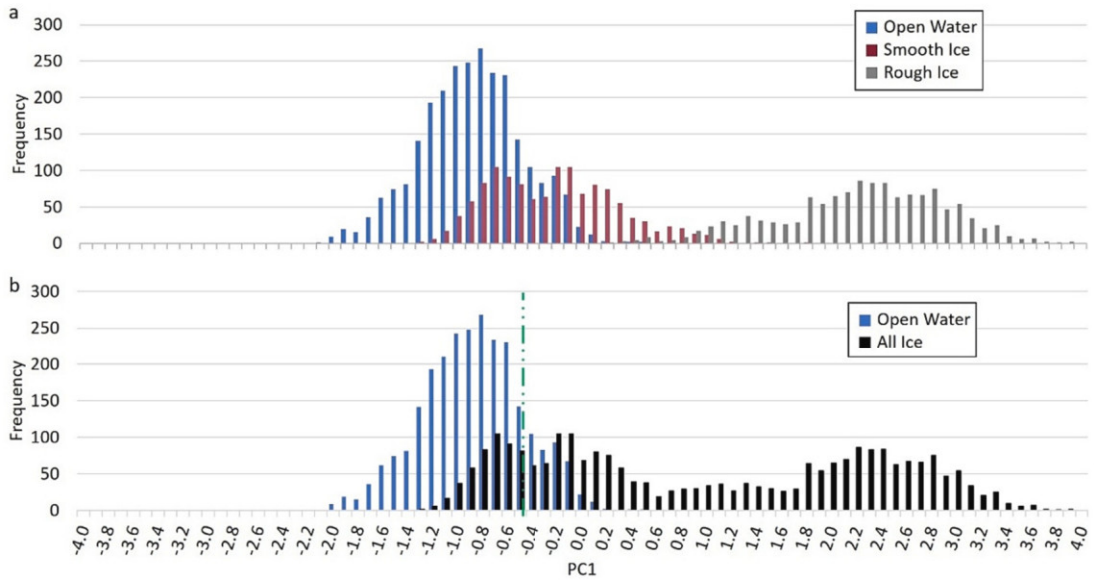

Fig. 8. Histogram of first principal component, PC1, for training data from four river reaches showing delineation between smooth and rough ice (a), as compared to open water. Smooth ice PC1 shows a bimodal distribution and a large overlap with open water (a). Panel b shows all ice (smooth and rough combined) with an equivalent number of open water pixels: green dashed line indicates the PC1 threshold (−0.4869) between ice and open water. (For interpretation of the references to colour in this figure legend, the reader is referred to the web version of this article.)

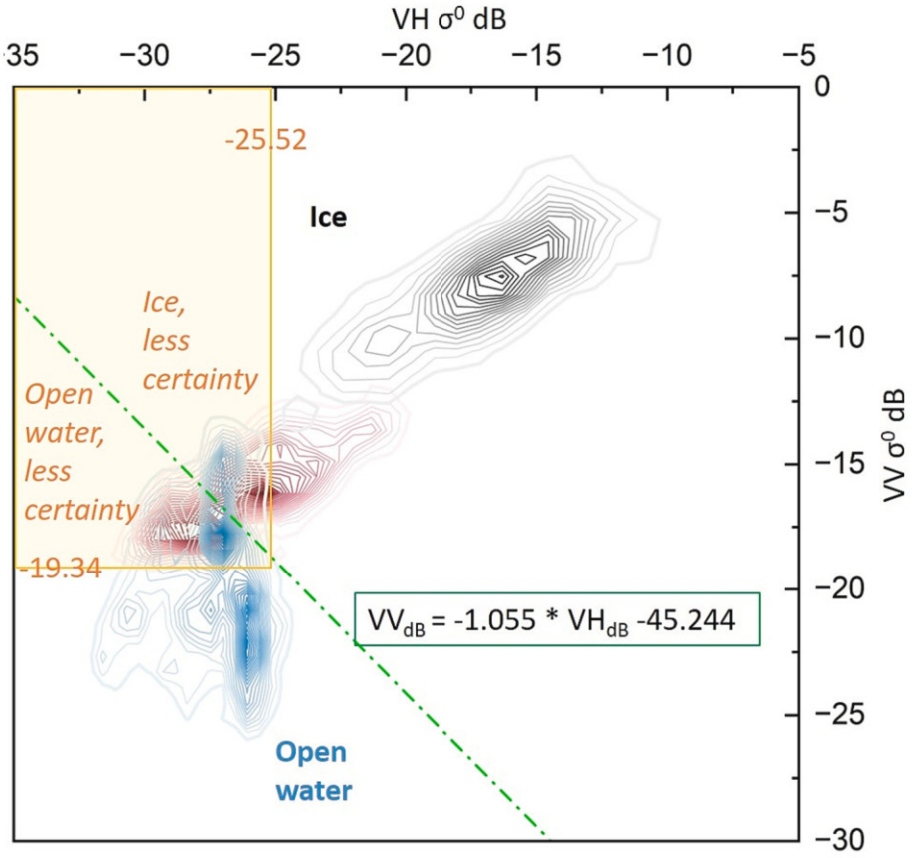

Fig. 9. Classification threshold for river ice vs. open water (green dashed line), based on PC1 equal-error analysis drawn over a kernel density plot where open water density shown by blue contours, smooth ice density by maroon contours, and rough ice density shown by black contours. Two optional "less-certainty" categories are outlined based on VV higher than 95% of all ice pixels and VH lower than 95% of open water pixels where VV satisfies the first condition. (For interpretation of the references to colour in this figure legend, the reader is referred to the web version of this article.)

Table 3
SAR classification accuracy for nine northern river reaches. Kappa statistic agreement is per Landis and Koch (1977).

Validation River Name	River Type[a]/ Width (m)	Glacial contribution	n validation cases	% false open water cases	% false ice cases	Overall Accuracy	Kappa Statistic	Kappa Statistic Agreement[b]
Colville	multi A/ 263	none	10	42%	25%	65%	0.31	fair
Kuskokwim	multi A/ 683	medium	17	44%	17%	71%	0.40	fair
Copper	multi B/ 260	high	36	9%	50%	69%	0.40	fair
Innoko	single M/ 186	low	18	45%	7%	69%	0.42	moderate
Yukon, P.	multi A/ 974	high	28	33%	8%	79%	0.58	moderate
Tanana	multi A/ 282	high	38	0%	50%	86%	0.59	moderate
Kantishna	multi A/ 181	medium	13	15%	17%	85%	0.61	substantial
Noatak	multi B/ 204	none	29	4%	23%	86%	0.73	substantial
Yukon, G.*	multi A/ 774	high	23	0%	21%	93%	0.84	almost perfect

[a] A = anastomosing, B = braided, M = meandering.
[b] Landis and Koch, 1977
* Indicates site was also used for training in previous winter.

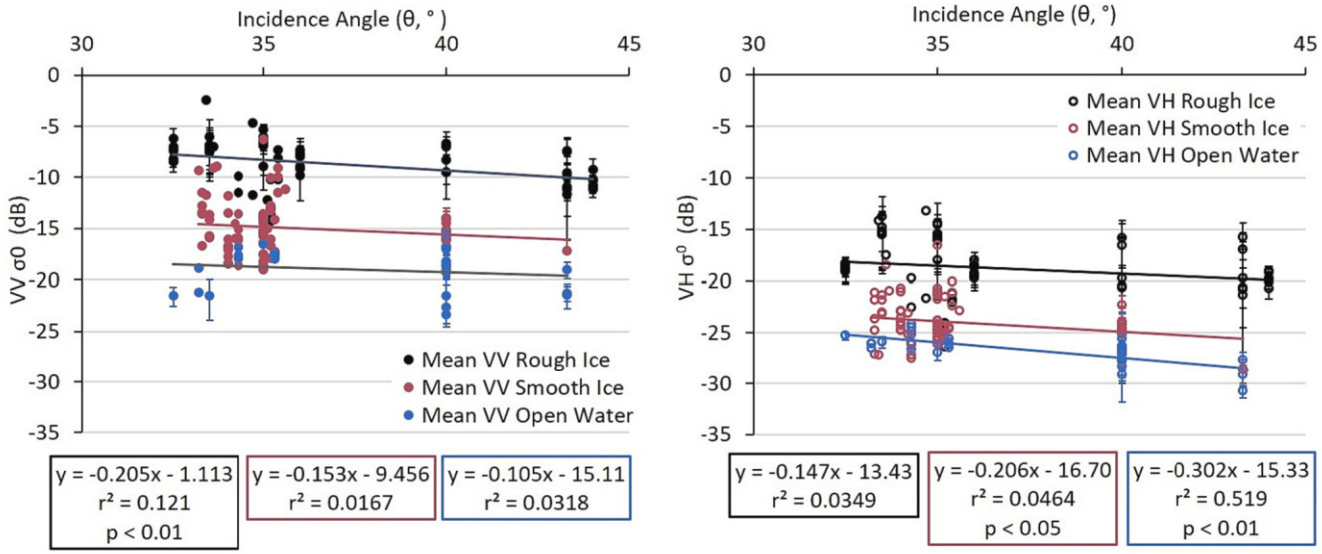

Fig. 10. Mean backscatter from VV (left panel) and VH (right panel) from shore-based camera field of views (FOVs) and field training points plotted against incidence angle of acquisition, show very shallow negative slopes, low r^2 values, and are statistically significantly correlated for three regressions. Error bars show standard deviation.

attributes (permafrost type, river morphology, glacial silt load, latitude, and river width) but did not find clear-cut relationships between types of rivers and classification accuracy: the classification performed moderately well or better for the majority (six out of nine) of the reaches we tested it on. The highest accuracy, (moderate to almost perfect agreement) was achieved in multi-channel rivers, although the single-channel river Innoko River also performed moderately well, but it should be noted that the majority of our samples were from multi-channel rivers (Table 3).

Once the ice in a river stops moving in early winter and creates a stationary cover, our C-band dual-pol river ice classification approach performed moderately well (Table 3, Fig. 11) and would be useful for travelers living in river-side communities. However, since pan ice has such a wide range of backscatter response, this classification should not be mis-used to gauge when a river freezes up and stops moving.

The Colville and Kuskokwim rivers had a high percentage of false open water pixel detection while the Copper River showed a high percentage of false ice classifications. We examine possible reasons for these results below.

4.3. Factors affecting classification accuracy

4.3.1. Accuracy and temporal offset

The temporal offset between observation and SAR acquisition may have impacted accuracy. SAR acquisition times were usually 3–4 h prior or 6–8 h after the shore-based camera image was taken, depending on whether the satellite was in ascending or descending flight geometry. This may have been a factor in classification accuracy for the Kuskokwim River near Napaskiak, which demonstrated fast changes by freezing and melting completely at least twice before finally developing a static ice cover.

4.3.2. False ice classification from open water at "rapids"

Fast water at river "rapids" (fast-flowing water with a rough surface) is most likely the cause of persistent false ice classifications from open water at the current-roughened reach of the Copper River in this study, causing high σ^0 in both VV and VH. This river carries a high glacial silt load, and visible riffles on the water surface in shore-based camera photos indicate high flow velocity. The VH σ^0 from open water on the Copper River at the fast-moving current-roughened reach was in the −22 dB to −25 dB range, well above most VH σ^0 for open water. This river never completely froze over, exhibiting an OWZ that persisted all winter in the fast-flowing main channel and was consistently misclassified as ice. Jasek et al. (2013), also saw confusion in their C-band classification between rough open water at river reaches known as "rapids" and ice. While VH shows less sensitivity to roughness, certain rough open-water conditions (possibly emergent rocks, whitecaps, or spray) seem to cause depolarization and therefore elevate VH σ^0. SAR

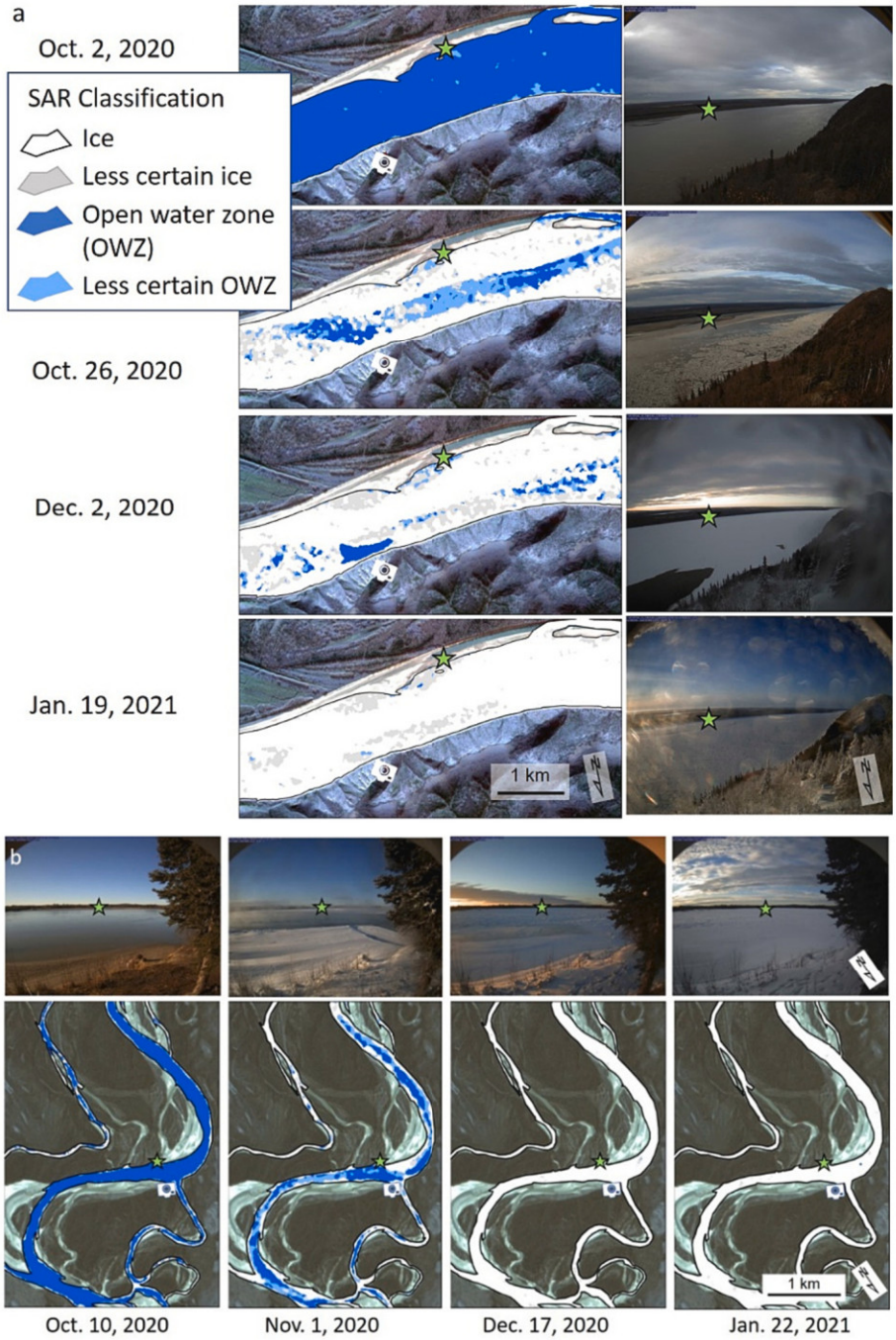

Fig. 11. Panel a shows the Yukon R. at Paimiut with SAR classification and shore-based camera for four dates, and panel b shows the Tanana River at Sam Charley Island, about 20 river km SW of Fairbanks with shore-based camera image on top row and SAR classification on bottom row. Camera icons indicate location of shore-based camera and green stars are in the same location in the vertical SAR-classification and the oblique photos. Background image in panel a is Planet Oct 14, 2020; in panel b is Planet Oct. 10, 2020. (For interpretation of the references to colour in this figure legend, the reader is referred to the web version of this article.)

classifications of river ice may be useful only in non-rapids river reaches, but further investigation is needed to identify conditions that increase VH σ^0 from "rapids".

4.3.3. *Potential controls of σ^0 from river ice*

4.3.3.1. Grounded ice. Clear, columnar river ice that freezes entirely to the river bed lacks the high dielectric contrast that exists at the ice/water interface and therefore bedfast ice returns a much lower σ^0 than ice overlying liquid water (Juhls et al., 2021). On the Colville River, false open water classification occurred in an area adjacent to the shore and a sandbar, which could indicate grounded ice in shallow water as a possible cause for low σ^0. The training area of smooth ice on the Kuskokwim River near Kwethluk (Fig. 4c, dotted black polygon; Fig. 6, lower left panel, red symbols) showing very low σ^0 is from an area close to shore lying outside the main river channel and could be grounded ice.

4.3.3.2. Backscatter from wet ice. Since σ^0 values from smooth open water are low, due to specular reflection where the microwave is reflected away from the sensor, we could expect low σ^0 in the case of water on top of ice (overflow). Yet, early winter overflow on ice as detected by shore-based cameras on three Alaska rivers, could not be differentiated

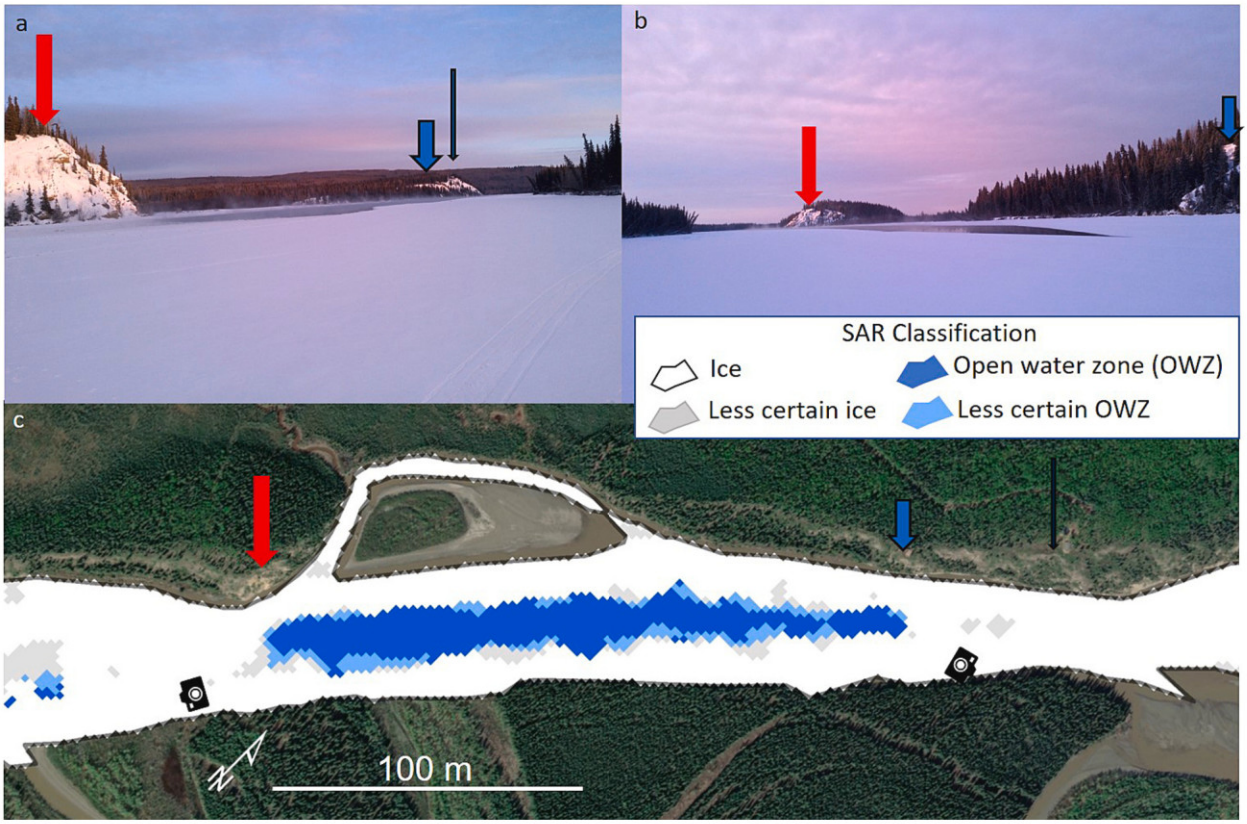

Fig. 12. Citizen science photos uploaded to the Fresh Eyes on Ice Observer (https://obs.feoi.axds.co/) showing a large OWZ still unfrozen on Dec. 20, 2020 on the Tanana R. near the Rosie Creek Trail (a,b). On-ice photo observations show perfect agreement with SAR classification from the same date (c). Red, blue, and black arrows point to the same landmarks in all panels for orientation between oblique view (a,b) and vertical view (c) of this river reach. Background image in lower panel Alaska High Resolution Imagery RGB 2020 (Maxar Technologies Inc., Alaska Geospatial Office, USGS), photo credit (a,b) C. Arp. (For interpretation of the references to colour in this figure legend, the reader is referred to the web version of this article.)

from dry ice with SAR. Both VV and VH σ^0 from overflow on rough ice, as noted by the Kuskokwim shore-based camera (Fig. 3d) was similar to dry rough ice, following results reported by Unterschultz et al. (2009). Since water is highly reflective, a thin coat of water on an ice surface would theoretically prohibit the SAR signal from penetrating the ice, reflecting the signal back to the satellite from a rough wet ice surface (for both VV and VH polarizations), or away from the satellite if the surface were smooth. Overflow on smooth ice would theoretically create a smooth surface similar to smooth open water and the SAR signal would be expected to be scattered away from the sensor, resulting in lower σ^0. Yet, as seen from the Innoko R. shore-based camera in Nov. 2019 was correctly classified as "ice". One explanation could be that the area of overflow was too small to show up, or that "smooth ice" has enough rough perturbations to create a rough surface when coated by a thin layer of water. Overflow under snow was detected on areas of Copper River ice, due to high position of shore-based camera which provided a more vertical view, but σ^0 from these areas were also high enough to be classified as ice, although the shore-based camera was too far away to determine the texture of the ice (smooth or rough) prior to overflow. We note these three cases of σ^0 from overflow on rough, smooth, and unknown textured ice being very similar to σ^0 dry ice. However, σ^0 from the Kuskokwim River near Napaskiak oscillated between low and high in the main river channel, and the shore-based camera here showed some re-frozen overflow. The intermittent low SAR σ^0 from this river reach could be explained by overflow with a smooth surface hidden under the snow causing false open water classification.

4.3.3.3. River flow velocity and frazil ice in and under ice cover. We noticed that VV σ^0 values were generally higher from ice in main, faster-flowing river channels whereas ice formed over slower currents tends to show lower σ^0 values. Higher-velocity channels tend to have a rougher top surface causing scattering at the air/ice interface from jumbled pan-ice which, although secondary to the scattering at the ice/water interface, still contributes to overall σ^0. Turbulence under the ice in fast-flowing channels could cause a rough water surface below the ice, which would increase σ^0, especially in VV polarization. Other reasons that ice in main fast-flowing channels have higher σ^0 could be super-cooled water from high-velocity flow creating small particles of frazil ice that adhere to the underside of the ice to potentially cause a rough ice/water interface (Fig. 1). Frazil ice are small ice crystals (0.001 to 10 mm, Svensson and Omstedt, 1994) formed in super-cooled, turbulent water. We have observed small particles (~ 8 mm) of frazil ice suspended in liquid water beneath well-formed ice covers (40–80 cm thick), on the Tanana River. Frazil ice can also make up a significant portion of a river ice cover, in contrast to columnar ice (Fig. 13b) which forms in low flow velocity regions of rivers with calm surfaces (Ashton, 1986). Ice crystal orientation in frazil ice and columnar ice is different, and may lead to higher backscatter from frazil ice than columnar ice.

4.3.3.4. Glacial silt frozen in river ice. The rivers with the highest accuracy, (moderate to almost perfect agreement) were multi-channel rivers, with the exception of the single-channel river Innoko River which showed moderate agreement (Table 3). Rivers with the highest accuracy carried some glacial silt load, with the exception of the Noatak River, that could create "dirty" ice (Fig. 13), possibly increasing SAR backscatter. Many northern rivers carry a high load of suspended glacial silt and sand (Chikita et al., 2002; Harrold and Burrows, 1983; Neill et al., 1984; Williams and Rosgen, 1989). While quantifying the glacial

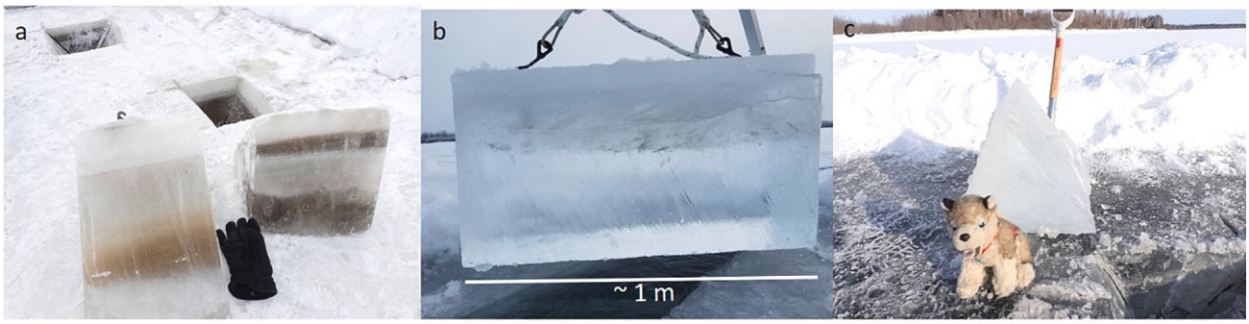

Fig. 13. Examples of varying glacial silt concentrations in Tanana River ice from "smooth" ice locations. Panel a) shows two samples relatively near each other with very different amount of frozen sediment/silt harvested near Nenana. Columnar ice block (b) harvested near Sam Charley Island shows no silt inclusion. Panel c) shows relatively clear ice harvested near Tolovana Roadhouse with no visible frozen sediment. (Photo credits: a,c: M. Engram, b: C. Arp.)

silt load is beyond the scope of this paper, we note that silt or sediment in ice could increase backscatter by increasing the dielectric constant of pure ice. Glacial rivers could therefore have a different backscatter threshold dividing ice and open water than clear-water rivers.

Flow velocity could interact with sediment load to influence σ^0 in river ice since swifter currents keep sediment suspended longer possibly leading to more particulate matter included in the ice. Conversely, a slower current would allow particles to settle prior to freezing, producing clearer ice. We noticed a large variation in the amount of sediment frozen in ice blocks we extracted ice from three "smooth ice" locations on the Tanana River, observing clear ice at two locations and sediment/silt frozen into the ice at the other (Fig. 13).

If dirty ice were a driver of σ^0, it would follow that ice which freezes earlier when glacial silt suspension loads are higher would include more silt and therefore have a higher σ^0 than later-freezing, cleaner ice. A large open water zone near Rosie Creek on the Tanana River didn't freeze until late December 2020 (Fig. 12). We compared the σ^0 at the Rosie Creek site from early and late-freezing ice across the channel (orthogonal to current) and along the channel (parallel to current). Although we did not extract an ice block at this location during fieldwork, sediment from glacial melt should lower as winter progresses. We saw much lower VH σ^0 in late-freezing ice in the central channel in January (~−20 to −24 dB) compared to VH σ^0 from early-freezing ice in the central channel (~ −8 to −13 dB) indicating that sediment frozen in the ice could be a control on VH σ^0. We did not see lower VV σ^0 from late-freezing ice in the main channel, indicating that sediment in the ice does not drive VV σ^0.

4.3.4. Smooth ice and open water backscatter overlap

We saw an overlap between backscatter from smooth ice and open water which impacted our ability to differentiate these classes (Fig. 9). Previous attempts at ice classification using SAR also reported an overlap between smooth ice and open water (de Roda Husman et al., 2021; Jasek et al., 2013). While we saw open water and ice as sometimes distinct within a river (Fig. 6, Yukon and Tanana rivers), our SAR classification produced cases of false open water at locations of smooth ice in slow-moving parts of rivers, especially on the Colville and Innoko rivers (Table 3).

Both VV and VH σ^0 values for smooth ice at the slow-moving, deep single-channel Innoko River were lower than those from rough ice on multi-channel rivers (Fig. 6). However, comparison of field observations on the Tanana River in Jan. 2021 to SAR showed smooth ice σ^0 as sometimes higher and sometimes lower than σ^0 from rough ice on that same river. This difference σ^0 at the location of smooth ice observed from above while standing on the river surface, indicates the air-ice interface is not the only factor affecting σ^0. Our top-of-ice field observations cannot determine whether the ice is columnar ice or if there is significant frazil ice within the ice column causing scattering from within the ice, and also could not perceive the roughness at the ice-water interface: this could be a source of the confusion between smooth and rough ice. Humans observe the top ice texture at the air/ice interface while SAR is reacting to the underside of the ice at the ice/water interface (Gherboudj et al., 2010) and could also be scattering from within the ice.

By determining our threshold between open water and ice along the axis of highest variability (PC1) between VH and VV polarizations for each pixel, we have developed a bi-conditional classification that slices through the smooth/open water overlap at a low-density area for both (Fig. 9). To acknowledge the uncertainty associated with the overlap between smooth ice and open water, we created parameters for less-certain ice and open water using statistics that consider both VV and VH intensities.

4.4. Imaging with different incidence angles and gamma-naught

Sentinel-1 has an incidence angle range from 29.1°-46°, and measurements from lab-grown ice (Leconte et al., 2009) and predictions from a river ice σ^0 model (Gherboudj et al., 2010) show only a slight decrease in σ^0 from clear ice over this range. Our results agree with these published results, showing only a slight (slopes from 0.1 to 0.3 dB) decrease of σ^0 from river ice with increasing incidence angle in both VV and VH polarizations (Fig. 10). The slopes are shallow and low Pearson's r statistics indicate weak correlations, although there is some statistical significance to the effect of incidence angle across a Sentinel-1 scene for rough ice in VV, and for smooth ice and open water in VH. This slight decrease in σ^0 for rough ice and open water have no effect on our classification since pixels showing this decrease would still be classified as "ice" and "water" respectively. Significance for the slight decrease in VH for smooth ice could be caused by having only a single sample at higher incidence angles (Fig. 10). While we conclude that this slight decrease in σ^0 with increasing incidence angle has negligible effect on the SAR ice classification, radiometrically flatter scenes can be obtained by using gamma-naught (γ^0) calibration. We therefore recommend using gamma-naught (γ^0), geometrically corrected with a digital elevation model, to produce a radiometrically flatter scene for future river ice analyses. There is also a trend in SAR application science toward providing ready-to-use radiometric terrain corrected products to SAR users (e.g., from the Alaska Satellite Facility), which are calibrated in γ^0. We have therefore included γ^0 thresholds in our supplementary material (Supplemental Fig. 1) and have published python code in GitHUB for both σ^0 and γ^0.

4.5. Future work

4.5.1. Determining depolarizing features and scattering mechanisms in river ice

We used top-of-ice observable features to categorize ice into "rough" and "smooth" and we see σ^0 from these two categories clustering in

density plots (Fig. 7b), indicating that these two categories are fairly useful. However, we see a wider spread of VH intensity values (>10 dB) compared to VV values (<10 dB) from "smooth" ice with two distinct density clusters (Fig. 7b). It would be pivotal to examine why VH is sometimes higher from ice; specifically, which features on, in, or under river ice cause depolarization of the vertical transmitted signal that results in higher VH σ^0. We could then determine the conditions when VH polarization can be accurately applied to classify ice and the scenarios where it is unreliable. It would also be useful to learn major causes of σ^0 for the VV polarization: we've suggested some drivers of C-band backscatter as frozen sediment in the ice, frazil ice sticking to the underside of high flow velocity channels, and frazil ice in the ice. Knowledge of the physical features that increase SAR scattering would be useful to further improve this C-band SAR river ice classification. Taking it one step further, using decomposed quadrature-polarized (quad-pol) C-band SAR to learn the scattering mechanism (single-bounce, double-bounce, or volumetric) over various targets coupled with ground truth could guide modification of the classification to fit different kinds of rivers.

4.5.2. L-band SAR

The upcoming NASA-ISRO SAR Mission (NISAR) planned to launch in 2024 will provide data with L-band (~24 cm) wavelength freely available to the scientific community. Future work in SAR river ice classification could include a multifrequency component, comparing or differencing C- and L-band backscatter to take advantage of different SAR wavelengths scattering from different sized targets. Quad-pol acquisitions are planned over limited northern areas, although generally NISAR will acquire dual-polarized data. Knowledge of scattering mechanisms and the different types of river ice that produce such scattering in L-band could be determined from polarimetric decomposition of quad-pol data and could be useful to interpret SAR backscatter from river ice.

4.5.3. Future field work

Future field work to sample and measure the possible controls of C-band backscatter from river ice would be an important step to improving SAR river ice classification. Location and extent of grounded ice, frazil ice in the ice column, frazil ice in suspension beneath ice cover, and flow velocity under the ice, would be helpful measurements to improve classification accuracy. Backscatter from grounded river ice needs further characterization with the goal to create a separate grounded-ice class to differentiate the low backscatter from grounded ice and open water. Measurements of sediment load frozen in river ice would be valuable data to compare to SAR backscatter as well as identification of sediment type (e.g., organic, glacial silt, algal): different types of impurities trapped in the ice will probably cause different σ^0 intensities, for example, frozen organic matter might not reflect C-band SAR while a certain percentage of glacial silt could increase σ^0. Identifying a reliable remote sensing proxy for each type of suspended sediment would be very useful input for customizing SAR σ^0 thresholds for different northern rivers. Mapping the extent and location of overflow, as well as observing and noting the roughness of liquid water surface would aid understanding of how overflow could affect a SAR fiver ice classification (and could also aid in the development of using SAR for overflow detection).

4.5.4. Observation guidelines for the future

Fixed shore-based camera and citizen scientist photos were very important in training and validating this classification and we learned that 1) camera positioning, 2) repeated photos, and 3) photos timed close to SAR overpass from citizen scientists are all important. Camera positioning from the most vertical angle possible would make comparison to remote sensing imaging easier and more accurate. Repeated photos at the same location over time improves our ability to validate remote sensing classifications. Optimal citizen science repeated observations would include "interesting" freeze-up (or break-up) photos, but also need to include observations of completely open water and complete ice cover to use for validation. The most useful observations are those timed to coincide with satellite overpasses: publishing satellite acquisition dates and times to rural northern communities could facilitate citizen science integration into remote sensing validation.

4.5.5. Determining persistent OWZs

Future work could also include performing this classification on rivers during previous years (2015-present) using Sentinel-1 data to create hazard maps of perennially open areas to avoid. These maps could be validated and built upon by local indigenous knowledge and provided to rural Alaska communities. As well as improving winter travel safety for rural Alaska community members, knowledge of river freeze-up timing and ice extent is important as a climate change indicator (Weltzin et al., 2020) and a SAR river-ice classification will provide important information on warming of the Arctic.

5. Conclusions

We present a SAR classification based on the first principal component (PC1) of both VV and VH intensity values for early winter river ice after a static ice cover has formed with fairly high confidence on large multi-channel rivers, and with the caveat that OWZs smaller or narrower than one 10 m pixel will probably not be detected. However, since pan ice has such a wide range of backscatter response, this classification should not be mis-used to gauge when a river freezes up and stops moving. Another limitation seems to be the inability to detect ice/ open water at high-turbulent "rapids" sections of rivers, although these sections could be masked out of a river ice map. Frequency of SAR acquisitions is also a limitation since acquisitions are not daily.

Overall accuracy of this classification for these northern rivers in early winter ranges from 65% to 93% resulting in $\widehat{K}$ statistics of 0.31–0.84 at nine reaches in eight Alaska rivers, with higher confidence for turbid/glacial-silt laden and faster-flowing main channels of rivers. Since channels of anastomosing rivers may be the most prone to open water because they are often steeper with higher turbulence, this SAR classification can show new hazardous reaches of an anastomosing river that may have been safe in the past. The incidence angle for σ^0 VV-VH dual-pol Sentinel-1 is not a factor in producing classification errors, but we recommend using radiometrically-flatter γ^0 for future work. The SAR classification may not by useful where there is grounded ice or in "rapids" sections of rivers, but further characterization of backscatter from these conditions could improve the classification. In addition to our first principal component SAR river ice classification, we present a large number of data points collected through remote sensing, fixed cameras, and citizen science from 12 reaches of eight rivers north of 60° N latitude which should prove valuable to other researchers. We anticipate this work to continue to develop toward map products to inform rural northern winter travelers of unsafe and changing conditions on river ice.

Funding

Funding for this work was provided by the National Science Foundation Navigating the New Arctic and Arctic Observing Network (Award # 1836523) through the Fresh Eyes on Ice project and by the National Aeronautics and Space Administration ROSES Citizen Science for Earth Systems Program (Award # 80NSSC21K0858] through the Community Eyes on River Ice project.

CRediT authorship contribution statement

Melanie Engram: Data curation, Formal analysis, Investigation, Methodology, Software, Validation, Visualization, Writing – original

draft, Writing – review & editing. **Franz J. Meyer:** Formal analysis, Methodology, Supervision. **Dana R.N. Brown:** Conceptualization, Writing – review & editing. **Sarah Clement:** Investigation, Writing – review & editing. **Allen C. Bondurant:** Investigation, Software, Writing – review & editing. **Katie V. Spellman:** Conceptualization, Funding acquisition, Supervision, Writing – review & editing. **Laura E. Oxtoby:** Writing – review & editing. **Christopher D. Arp:** Conceptualization, Funding acquisition, Investigation, Project administration, Supervision, Writing – review & editing.

Declaration of competing interest

The authors declare that they have no known competing financial interests or personal relationships that could have appeared to influence the work reported in this paper.

Data availability

All data used are publicly available: specific data granules are specified in the Supplementary Information for the manuscript. Python code to implement classification are published in GitHub: melanie-engram/C-band_SAR_Rver_Ice_vs_OpenWater_classification/.

Acknowledgements

We thank Alaska citizen scientists including students and teachers in many schools participating in the Fresh Eyes on Ice project for sharing photo observations during the river freeze-up period. Koyukuk National Wildlife Refuge (USFWS), Bethel Search and Rescue, especially C. Guest, the Native Village of Noatak and Napaaqtugmiut School, Bonanza Creek LTER, the Native Village of Shageluk and Innoko River School, the Native Village of Bethel and Bethel Regional High School, the Native Village of Napaskiak and Earl Samuelson, the communities of Galena, Fairbanks, Tazlina, and the Alaska Dept. of Fish and Game Division of Commercial Fisheries for guidance, permission, and site access for shore-mounted time-lapse cameras. The authors gratefully acknowledge the Alaska Satellite Facility for providing SAR data and the European Space Agency for providing Sentinel-2 imagery and post-processing software and elevation data for terrain correction.

Appendix A. Supplementary data

Supplementary data to this article can be found online at https://doi.org/10.1016/j.rse.2024.114096.

References

Ansari, S., Rennie, C.D., Seidou, O., Malenchak, J., Zare, S.G., 2017. Automated monitoring of river ice processes using shore-based imagery. Cold Reg. Sci. Technol. 142, 1–16.

Ashton, G.D., 1986. Chapter 2, ice physics. In: Ashton, G.D. (Ed.), River & Lake ice Engineering. Water Resources Publications, LLC, Littleton, Colorado, USA, pp. 26–29.

Bartsch, A., Pointner, G., Leibman, M.O., Dvornikov, Y.A., Khomutov, A.V., Trofaier, A. M., 2017. Circumpolar mapping of ground-fast Lake ice. Front. Earth Sci. 5, 12. https://doi.org/10.3389/feart.2017.00012.

Bondurant, A., Arp, C., Brown, D., Spellman, K., 2022. Alaska River ice phenology camera network - 2019-2022. Arctic Data Center (urn:uuid:edbc8d9e-42f9-4f76-bea3-4e59ef48294d).

Brabets, T.P., Walvoord, M.A., 2009. Trends in streamflow in the Yukon River basin from 1944 to 2005 and the influence of the Pacific decadal oscillation. J. Hydrol. 371 (1–4), 108–119. https://doi.org/10.1016/j.jhydrol.2009.03.018.

Brown, D.R.N., Brinkman, T.J., Verbyla, D.L., Brown, C.L., Cold, H.S., Hollingsworth, T. N., 2018. Changing river ice seasonality and impacts on interior Alaskan communities. Weath. Clim. Soc. 10 (4), 625–640. https://doi.org/10.1175/WCAS-D-17-0101.1.

Brown, D.R.N., Arp, C.D., Brinkman, T.J., Cellarius, B.A., Engram, M., Miller, M.E., Spellman, K.V., 2023. Long-term change and geospatial patterns of river ice cover and navigability in southcentral Alaska detected with remote sensing. Arct. Antarct. Alp. Res. 55 (1), 2241279. https://doi.org/10.1080/15230430.2023.2241279.

Chikita, K.A., Kemnitz, R., Kumai, R., 2002. Characteristics of sediment discharge in the subarctic Yukon River, Alaska. CATENA 48 (4), 235–253. https://doi.org/10.1016/S0341-8162(02)00032-2.

Cold, H.S., Brinkman, T.J., Brown, C.L., Hollingsworth, T.N., Brown, D.R.N., Heeringa, K. M., 2022. Assessing vulnerability of subsistence travel to effects of environmental change in interior Alaska. Ecol. Soc. 25 (1), 20. https://doi.org/10.5751/ES-11426-250120.

DGGS Staff, . Elevation Datasets of Alaska: Alaska Division of Geological & Geophysical Surveys Digital Data Series 4. https://elevation.alaska.gov. https://doi.org/10.14509/25239.

Eicken, H., Danielsen, F., Sam, J.-M., Fidel, M., Johnson, N., Poulsen, M.K., Lee, O.A., Spellman, K.V., Iversen, L., Pulsifer, P., 2021. Connecting top-down and bottom-up approaches in environmental observing. Bioscience 71 (5), 467–483. https://doi.org/10.1093/biosci/biab018.

Engram, M., Arp, C.D., Jones, B.M., Ajadi, O.A., Meyer, F.J., 2018. Analyzing floating and bedfast lake ice regimes across Arctic Alaska using 25 years of space-borne SAR imagery. Remote Sens. Environ. 209, 660–676. https://doi.org/10.1016/j.rse.2018.02.022.

Gauthier, Y., Weber, F., Savary, S., Jasek, M., Paquet, L.-M., Bernier, M., 2006. A combined classification scheme to characterise river ice from SAR data. A combined classification scheme to characterise river ice from SAR data. EARSeL eProceed. 5 (1), 77–88.

Gauthier, Y., Tremblay, M., Bernier, M., Furgal, C., 2010. Adaptation of a radar-based river ice mapping technology to the Nunavik context. Can. J. Remote. Sens. 36 (sup1), S168–S185.

Ge, S., Yang, D., Kane, D.L., 2013. Yukon River basin long-term (1977–2006) hydrologic and climatic analysis. Hydrol. Process. 27 (17), 2475–2484.

Gherboudj, I., Bernier, M., Leconte, R., 2010. A backscatter modeling for river ice: analysis and numerical results. IEEE Trans. Geosci. Remote Sens. 48, (4), 1788–1798. https://doi.org/10.1109/tgrs.2009.2034256.

Goldstream Group, 2022. Fresh Eyes on Ice: Assessment of the River Ice Information Needs of Alaskans. Fairbanks, Alaska. http://freshEyesonice.org/media/1415/fresh-eyes-on-ice-needs-assessment-goldstream-group-2022.pdf.

Guest, C., 2019. Aerial Observations of Kuskokwim River, 18-Nov and 3-Dec 2019. Open water zones at head of Kuskokwak off the Kuskokwim River upstream of Kwethluk taken during Bethel Search and Rescue flight. https://obs.feoi.axds.co/observations/6. https://obs.feoi.axds.co/observations/7.

Harrold, P.E., Burrows, R.L., 1983. Sediment transport in the Tanana River near Fairbanks, Alaska, 1982. In: Survey, U.G. (Ed.), US Department of the Interior, Geological Survey Water-Resources Investigations Report 83–4213.

Herman-Mercer, N., Schuster, P., Maracle, K.T., 2011. Indigenous observations of climate change in the lower Yukon River basin, Alaska. Hum. Organ. 70, (3), 244–252. https://doi.org/10.17730/humo.70.3.v88841235897071m.

Hinzman, L.D., Bettez, N.D., Bolton, W.R., Chapin, F.S., Dyurgerov, M.B., Fastie, C.L., Griffith, B., Hollister, R.D., Hope, A., Huntington, H.P., Jensen, A.M., Jia, G.J., Jorgenson, T., Kane, D.L., Klein, D.R., Kofinas, G., Lynch, A.H., Lloyd, A.H., McGuire, A.D., Nelson, F.E., Oechel, W.C., Osterkamp, T.E., Racine, C.H., Romanovsky, V.E., Stone, R.S., Stow, D.A., Sturm, M., Tweedie, C.E., Vourlitis, G.L., Walker, M.D., Walker, D.A., Webber, P.J., Welker, J.M., Winker, K., Yoshikawa, K., 2005. Evidence and implications of recent climate change in northern Alaska and other arctic regions. Clim. Chang. 72 (3), 251–298. https://doi.org/10.1007/s10584-005-5352-2.

Jasek, M., Gauthier, Y., Poulin, J., Bernier, M., 2013. Monitoring of freeze-up on the Peace River at the vermilion rapids using RADARSAT-2 SAR data. In: Committee on River Ice Processes and the Environment, 17th Workshop on River Ice, Edmonton, Alberta, pp. 21–24.

Jorgenson, T., Yoshikawa, K., Kanevskiy, M., Shur, Y., Romanovsky, V., Marchenko, S., Grosse, G., Brown, J., Jones, B., 2008. Permafrost characteristics of Alaska. In: Proceedings of the Ninth International Conference on Permafrost (eds. Kane, D. L. & Hinkel, K. M.) map in scale 1 :7,000,000 (Institute of Northern Engineering, Fairbanks, 2008).

Juhls, B., Antonova, S., Angelopoulos, M., Bobrov, N., Grigoriev, M., Langer, M., Maksimov, G., Miesner, F., Overduin, P.P., 2021. Serpentine (floating) ice channels and their interaction with riverbed permafrost in the Lena River Delta, Russia. Front. Earth Sci. 9 https://doi.org/10.3389/feart.2021.689941.

Knoll, L.B., Sharma, S., Denfeld, B.A., Flaim, G., Hori, Y., Magnuson, J.J., Straile, D., Weyhenmeyer, G.A., 2019. Consequences of lake and river ice loss on cultural ecosystem services. Limnol. Oceanogr. Lett. 4 (5), 119–131. https://doi.org/10.1002/lol2.10116.

Landis, J.R., Koch, G.G., 1977. The measurement of observer agreement for categorical data. Biometrics 33 (1), 159–174.

Leconte, R., Daly, S., Gauthier, Y., Yankielun, N., Bérubé, F., Bernier, M., 2009. A controlled experiment to retrieve freshwater ice characteristics from an FM-CW radar system. Cold Reg. Sci. Technol. 55 (2), 212–220. https://doi.org/10.1016/j.coldregions.2008.04.003.

Lee, J.-S., Wen, J.-H., Ainsworth, T.L., Chen, K.-S., Chen, A.J., 2009. Improved sigma filter for speckle filtering of SAR imagery. IEEE Trans. Geosci. Remote Sens. 47 (1), 202–213. https://doi.org/10.1109/TGRS.2008.2002881.

Lindenschmidt, K.E., 2020. River Ice Processes and Ice Flood Forecasting. Springer, Cham, Switzerland. https://doi.org/10.1007/978-3-030-28679-8.

Lindenschmidt, K.E., Li, Z., 2018. Monitoring river ice cover development using the Freeman–Durden decomposition of quad-pol Radarsat-2 images. J. Appl. Remote. Sens. 12 (2), 026014.

Long, D.G., Collyer, R., Arnold, D.V., 1996. Dependence of the normalized radar cross section of water waves on Bragg wavelength-wind speed sensitivity. IEEE Trans. Geosci. Remote Sens. 34 (3), 656–666. https://doi.org/10.1109/36.499745.

Łoś, H., Osińska-Skotak, K., Pluto-Kossakowska, J., Bernier, M., Gauthier, Y., Jasek, M., Roth, A., 2016. Comparison of c-Band and x-Band Polarimetric SAR Data for River ice Classification on the Peace River. International Archives of the Photogrammetry, Remote Sensing & Spatial Information Sciences, p. 41.

Łoś, H., Osińska-Skotak, K., Pluto-Kossakowska, J., Bernier, M., Gauthier, Y., Pawłowski, B., 2019. Performance evaluation of quad-pol data compare to dual-pol SAR data for river ice classification. Eur. J. Remote Sens. 52 (sup1), 79–95.

Makaske, B., 2001. Anastomosing rivers: a review of their classification, origin and sedimentary products. Earth Sci. Rev. 53 (3), 149–196. https://doi.org/10.1016/S0012-8252(00)00038-6.

Mätzler, C., Wegmüller, U., 1987. Dielectric properties of fresh-water ice at microwave frequencies. J. Phys. D. Appl. Phys. 21 (11), 1623–1630.

Mermoz, S., Allain, S., Bernier, M., Pottier, E., Gherboudj, I., 2009. Classification of river ice using polarimetric SAR data. Can. J. Remote. Sens. 35 (5), 460–473. https://doi.org/10.5589/m09-034.

Meyer, F., 2019. Spaceborne Synthetic Aperture Radar: Principles, Data Access, and Basic Processing Techniques. Synthetic Aperture Radar (SAR) Handbook: Comprehensive Methodologies for Forest Monitoring and Biomass Estimation, pp. 21–64.

Neill, C.R., Buska, J.S., Chacho, E.F., Collins, C.M., Gatto, L.W., 1984. Overview of Tanana River Monitoring and Research Studies near Fairbanks, Alaska. Cold Regions Research and Engineering Laboratory (US). SR-84-37. https://hdl.handle.net/11681/11986.

Planet Team, 2017. Planet Application Program Interface. In Space for Life on Earth, San Francisco, CA.

Prowse, T., Alfredsen, K., Beltaos, S., Bonsal, B.R., Bowden, W.B., Duguay, C.R., Korhola, A., McNamara, J., Vincent, W.F., Vuglinsky, V., Anthony, K.M.W., Weyhenmeyer, G.A., 2011. Effects of changes in Arctic Lake and river ice. AMBIO: J. Human Environ. 40 (sp1), 63–74. https://doi.org/10.1007/s13280-011-0217-6.

de Roda Husman, S., van der Sanden, J.J., Lhermitte, S., Eleveld, M.A., 2021. Integrating intensity and context for improved supervised river ice classification from dual-pol Sentinel-1 SAR data. Int. J. Appl. Earth Obs. Geoinf. 101, 102359 https://doi.org/10.1016/j.jag.2021.102359.

Romanovsky, V.E., Smith, S.L., Christiansen, H.H., 2010. Permafrost thermal state in the polar northern hemisphere during the international polar year 2007-2009: a synthesis. Permafr. Periglac. Process. 21 (2), 106–116.

Schneider, W.S., Brewster, K., Kielland, K., Jones, C.E., 2013. On dangerous ice: Changing ice conditions on the Tanana River. University of Alaska Fairbanks, Oral History Program, Elmer E. Rasmuson Library and the Institute of Arctic Biology.

Skolunov, A.V., 1997. Frequency-temperature curve of the complex dielectric constant and refractive index of water. Fibre Chem. 29 (6), 367–373. https://doi.org/10.1007/BF02418871.

Small, D., 2011. Flattening gamma: radiometric terrain correction for SAR imagery. IEEE Trans. Geosci. Remote Sens. 49 (8), 3081–3093. https://doi.org/10.1109/TGRS.2011.2120616.

Stonevicius, E., Uselis, G., Grendaite, D., 2022. Ice detection with Sentinel-1 SAR backscatter threshold in long sections of temperate climate rivers. Remote Sens. 14 (7) https://doi.org/10.3390/rs14071627.

Svensson, U., Omstedt, A., 1994. Simulation of supercooling and size distribution in frazil ice dynamics. Cold Reg. Sci. Technol. 22 (3), 221–233. https://doi.org/10.1016/0165-232X(94)90001-9.

Torres, R., Snoeij, P., Geudtner, D., Bibby, D., Davidson, M., Attema, E., Potin, P., Rommen, B., Floury, N., Brown, M., 2012. GMES Sentinel-1 mission. Remote Sens. Environ. 120, 9–24. https://doi.org/10.1016/j.rse.2011.05.028.

Unterschultz, K.D., van der Sanden, J., Hicks, F.E., 2009. Potential of RADARSAT-1 for the monitoring of river ice: results of a case study on the Athabasca River at Fort McMurray, Canada. Cold Reg. Sci. Technol. 55 (2), 238–248. https://doi.org/10.1016/j.coldregions.2008.02.003.

Van der Sanden, J.J., Drouin, H., 2011. Satellite SAR observations of river ice cover: A RADARSAT-2 (C-band) and ALOS PALSAR (L-band) comparison. In: Proceedings of the 16th Workshop on River Ice, Winnipeg, MB (pp. 18-22).

Van der Sanden, J.J., Drouin, H., Geldsetzer, T., 2021. An automated procedure to map breaking river ice with C-band HH SAR data. Remote Sens. Environ. 252, 112119.

Walvoord, M.A., Striegl, R.G., 2007. Increased groundwater to stream discharge from permafrost thawing in the Yukon River basin: potential impacts on lateral export of carbon and nitrogen. Geophys. Res. Lett. 34 (12) https://doi.org/10.1029/2007GL030216.

Weber, F., Nixon, D., Hurley, J., 2003. Semi-automated classification of river ice types on the Peace River using RADARSAT-1 synthetic aperture radar (SAR) imagery. Can. J. Civ. Eng. 30 (1), 11–27.

Weltzin, J.F., Betancourt, J.L., Cook, B.I., Crimmins, T.M., Enquist, C.A.F., Gerst, M.D., Gross, J.E., Henebry, G.M., Hufft, R.A., Kenney, M.A., Kimball, J.S., Reed, B.C., Running, S.W., 2020. Seasonality of biological and physical systems as indicators of climatic variation and change. Clim. Chang. 163 (4), 1755–1771. https://doi.org/10.1007/s10584-020-02894-0.

White, D.M., Prokein, P., Chambers, M., Lilly, M.R., Toniolo, H., 2008. Use of synthetic aperture radar for selecting Alaskan lakes for winter water use. J. Am. Water Resour. Assoc. 44 (2), 276–284. https://doi.org/10.1111/j.1752-1688.2007.00160.x.

Williams, G.P., Rosgen, D.L., 1989. Measured Total Sediment Loads (Suspended Loads and Bedloads) for 93 United States Streams. US Geological Survey, Washington, DC. Report 89-67. https://pubs.usgs.gov/of/1989/0067/report.pdf.

Wilson, N.J., Walter, M.T., Waterhouse, J., 2015. Indigenous knowledge of hydrologic change in the Yukon River basin: a case study of ruby, Alaska. Arctic 68, (1), 93–106. https://doi.org/10.14430/arctic4459.

Yang, R.-M., Zhang, T., 2022. Dramatic thinning of Alaskan river ice and its climatic controls. Adv. Clim. Chang. Res. https://doi.org/10.1016/j.accre.2022.08.001.

Yang, X., Pavelsky, T.M., Allen, G.H., 2020. The past and future of global river ice. Nature 577 (7788), 69–73. https://doi.org/10.1038/s41586-019-1848-1.